# Compressible f-plane Solutions to Local Body Forces and Heatings; Part II: Gravity Wave, Acoustic Wave, and Mean Responses

Sharon L. Vadas,[1]

NorthWest Research Associates, CoRA div., 3380 Mitchell Lane, Boulder, CO, USA

Keywords: body force, heating, dynamics, gravity waves

## Abstract

In Part I, we derived the $f$-plane, compressible, linear solutions to horizontal and vertical body forces and heatings. In this companion paper, we apply our solutions to important examples of body forcings and heatings in our atmosphere. This includes wave breaking near the mesopause, geostrophic adjustment, thermospheric body forces from gravity wave (GW) dissipation, convective overshoot, and auroral heating. For each example, we calculate 1) the compressible and Boussinesq GW spectra, and 2) the GW perturbations at much higher altitudes. We also calculate the acoustic wave (AW) perturbations for three of these examples. We find that the compressible GW solutions are nearly identical to the Boussinesq solutions when the depth of the forcing/heating is less than the density scale height, $\mathcal{H}$. When the depth is greater than $\mathcal{H}$, the GW solutions are similar only when the GW vertical wavelengths are small, $\lambda_z \ll 4\pi\mathcal{H}$, where $\mathcal{H}$ is the density scale height. We find that the compressible solutions are needed to describe those GWs with $\lambda_z \gtrsim 2\pi\mathcal{H}$ excited by wave breaking near the mesopause, thermospheric body forces, and convective overshoot. The compressible solutions are always needed to describe the AWs. Body forcings/heatings with durations of $\chi \gg 5$ min can excite GWs with intrinsic periods $\tau_{Ir} > \chi/2$, but excite AWs with very small amplitudes. Body forcings/heatings with durations of $\chi \lesssim 10 - 20$ min can excite GWs and AWs efficiently.

[1]Corresponding author: Sharon Vadas, CoRA, 3380 Mitchell Lane, Boulder, CO, 80301, USA, W (303)415-9701x202, F (303)415-9702, vasha@cora.nwra.com

## 1. Introduction

Local, interval body forces and heatings describe the effects of outside processes on a local fluid. Here "local" describes a localized region in space, and "interval" describes a finite duration in time. These forcings/heatings can describe some of the effects of wave breaking, wave dissipation, convective overshoot, auroral heating, and geostrophic adjustment. These forcings/heatings excite GWs and AWs, and may induce mean winds and temperatures. Both the temporal and spatial characteristics of a forcing/heating determines the wave responses (Vadas and Fritts, 2001; Vadas *et al.*, 2003, hereafter VF01 and V03).

Local, interval horizontal body forces are wave-averaged, horizontal accelerations of the neutral fluid. They can be caused by wave breaking, wave dissipation, or geostrophic adjustment, to name a few. One important example arises near the mesopause from the breaking of GWs (Fritts and Alexander, 2003 and references therein; Fritts *et al.*, 2006). In the winter, mountain waves can propagate to near the mesopause, where they break and deposit their momentum (Plougonven *et al.*, 2008). During the spring, summer and fall, some GWs excited by deep convective overshoot can propagate to the mesopause; those with $10 < \lambda_H < 50$ km can break there (Holton and Alexander, 1999; Horinouchi *et al.*, 2002). These horizontal body forces close the jets near the mesopause (which would exist in thermal equilibrium), because they create a mean wind in the direction of GW propagation. This cools the summer mesopause because of an induced residual circulation (Nastrom et al., 1982; Holton, 1982, 1983; Dunkerton, 1982; Garcia, 1987). These body forces also excite "secondary" GWs (Dickinson, 1969; Blumen, 1972; Walterscheid and Boucher, 1984; Zhu and Holton, 1987; Fritts and Luo, 1992; Luo

and Fritts, 1993; Medvedev and Gavrilov, 1995; VF01; V03). These waves are dubbed "secondary" because they arise in response to the breaking of "primary" waves.

Some of the primary GWs from convection, and some of the secondary GWs from wave breaking near the mesopause, can propagate into the thermosphere and dissipate/break there (Vadas, 2007; Fritts and Vadas, 2008, hereafter V07 and FV08). These GWs typically have $\lambda_H > 20$ km. This creates thermospheric horizontal body forces (Hines, 1972; Vadas and Fritts, 2004, 2006, hereafter VF04 and VF06). Because of wind filtering in the lower thermosphere, those GWs tend to propagate against the background wind prior to breaking/dissipating (Hines and Reddy, 1967; Cowling *et al.*, 1971, Waldock and Jones, 1984,1986; Crowley *et al.*, 1987; FV08; Miyoshi and Fujiwara, 2008). Therefore, the body forces, which are orientated in the direction of wave propagation, depend on the tidal and planetary winds in the lower thermosphere (VL09). A recent study showed that thermospheric body forces excite secondary GWs and induce large mean winds of $200 - 400$ m/s in the force region (Vadas and Liu, 2009, hereafter VL09).

Local, interval vertical body forces can be used to describe the overshoot of the tropopause by deep convective plumes (Stull, 1976; VF04; Vadas and Fritts, 2009, hereafter VF09). Convective overshoot excites high frequency GWs with $\lambda_H =$ a few to $\sim 350$ km and with periods less than an hour. This process can alternatively be described as a localized heating in the stratosphere (Alexander *et al.*, 1995; Walterscheid *et al.*, 2001; Beres, 2004). Local, interval heatings can also describe the Joule heating that accompanies the aurora at $z \sim 120 - 140$ km (Hocke and Schlegel, 1996; Hocke *et al.*, 1996; Richmond, 1978; Hickey and Cole, 1988).

Mean and GW solutions for localized, interval heatings and body forcings were derived in the Boussinesq approximation (VF01). These solutions are valid when $\lambda_z \ll 4\pi\mathcal{H}$. Compressible effects are expected to be important 1) for forcings/heatings deeper than the density scale height $\mathcal{H}$, and 2) for GWs with $\lambda_z \gtrsim \pi\mathcal{H}$. However, these latter GWs

are precisely the GWs which penetrate deeply into the thermosphere (V07), and create large mean winds and secondary GWs upon dissipating there (VL09). These latter GWs may also seed plasma instabilities (Kelley, 1989; Fritts *et al.*, 2008; Takahashi *et al.*, 2009; Makela,*et al.*, 2010). In order to address this concern, Vadas (2010) derived the compressible $f$-plane linear solutions to localized, interval body forcings and heatings. This paper is the second in this 2-part series. The purpose of this paper is to apply these new solutions to 5 important examples of body forcings and heatings in our atmosphere. We organize this paper as follows. Sec. 2 gives a brief summary of the definitions and terms needed for this paper. In Sec. 3, we show the solutions for important horizontal body forces, namely wave breaking near the mesopause, geostrophic adjustment, wave dissipation in the thermosphere. Sec. 4 show the solutions for an important vertical body force, deep convective overshoot. Sec. 5 show the solutions for auroral heatings. Sec. 6 contains our conclusions.

## 2. Functions and definitions

The body forcing and heating functions are $\mathbf{F}(\mathbf{x})\mathcal{F}(t)$ and $J(\mathbf{x})\mathcal{F}(t)$, respectively. These functions are added to the right-hand-sides of the momentum and energy equations, respectively, as described in Vadas (2010). These functions have time dependence $\mathcal{F}(t)$; this function turns on and off smoothly in time for the finite time interval $\chi$, in order to represent the temporal evolution of realistic body forcings and heatings:

$$\mathcal{F}(t) = \frac{1}{\chi} \begin{cases} (1 - \cos \hat{a}t) & \text{for } 0 \leq t \leq \chi, \\ 0 & \text{for } t \leq 0 \text{ and } t \geq \chi. \end{cases} \tag{1}$$

The interval forcing/heating lasts from $t = 0$ to $\chi$, and has a frequency, $\hat{a}$, of

$$\hat{a} \equiv 2\pi n/\chi. \tag{2}$$

The number of cycles within the total duration $\chi$ is $n = 1, 2, 3, ...$, where $n$ is a positive integer. If $n = 1$, then only a single forcing/heating occurs. An impulsive forcing is a

special case of this more general forcing, and is obtained by setting $n = 1$ and $\chi \to 0$. For all of the examples in this paper, we set $n = 1$.

The spatial portion of the 3D body force is $\mathbf{F}(\mathbf{x}) = F_x(\mathbf{x})\hat{i} + F_y(\mathbf{x})\hat{j} + F_z(\mathbf{x})\hat{k}$, where $\hat{i}$, $\hat{j}$ and $\hat{k}$ are the zonal, meridional, and vertical unit vectors, respectively. The spatial portion of the heating is $J(\mathbf{x})$. These spatial distributions can be any arbitrary functions of $(x, y, z)$, although they and their spatial derivatives must be continuous functions of $x$, $y$, and $z$. We refer to these body forcings and heatings as "sources", because they excite GWs and AWs and generate mean winds and temperatures. The compressible, $f$-plane solutions to these body forces and heatings are linear, and assume that the background fluid is isothermal, non-dissipative, and unsheared. See Vadas (2010) for further details.

## 3. Wave and Mean Responses to Horizontal Body Forces

Horizontal body forces can be used to model many physical processes in our atmosphere. Here, we discuss 3 important examples.

*1. Wave breaking near the mesopause*

When GWs break near the mesopause, they create small-scale waves and wave motions (Taylor and Hapgood, 1990; Taylor *et al.*, 1995; Holton and Alexander, 1999; Andreassen *et al.*, 1998; Fritts *et al.*, 1998; Nakamura *et al.*, 1999; Yamada *et al.*, 2001; Fritts *et al.*, 2002; Hecht, 2004; Li *et al.*, 2005). They also deposit momentum into the background fluid on spatial scales of order the wavelengths and periods of the breaking waves in the packet (Fritts *et al.*, 2006). This deposition creates a horizontal body force in the direction of wave propagation. The zonal body force is the vertical flux of zonal momentum:

$$F_x\mathcal{F} = -\frac{1}{\overline{\rho}}\frac{\partial(\overline{\rho}\ \overline{u'w'^*})}{\partial z} \tag{3}$$

(Andrews *et al.*, 1987), where the overline denotes an average over 1-2 wave period and wavelengths. Additionally, $u'$, $v'$, and $w'$ are the zonal, meridional, and vertical velocity

perturbations, respectively, and $^*$ denotes the complex conjugate. For a saturated wave, $\overline{u'w'^*}$ is approximately constant (Lindzen, 1981). Eq. (3) then becomes

$$F_x \mathcal{F} \simeq \frac{\overline{u'w'^*}}{\mathcal{H}}. \tag{4}$$

As an example, we model the acceleration created by a packet of eastward-propagating convectively-generated GWs with $\lambda_x = 30$ km, $\lambda_z = 15$ km, ground-based period $\tau_r \equiv 2\pi/\omega_r = 10$ min, $u' = 40$ m/s, and $w' = 20$ m/s. Here, $\lambda_x = 2\pi/k$, $\lambda_y = 2\pi/l$, and $\lambda_z = 2\pi/m$ are the zonal, meridional, and vertical wavelengths, respectively, $(k, l, m)$ is the wavenumber vector, and $\omega_r$ is the observed frequency. These GWs break at $z = 85$ km. Additionally, we assume that the background zonal and meridional winds are $\overline{U} = 10$ m/s and $\overline{V} = 0$, respectively, $\mathcal{H} = 7$ km, $N_B = 0.02$ rad/s, $\gamma = 1.4$, $\mathrm{X_{MW}} = 30$, $g = 9.5$ m/s$^2$, a background temperature of $\overline{T} = 245$ K, and $f = 0$. Here, $\mathrm{X_{MW}}$ is the average molecular weight, and $f = 2\Omega \sin(\theta)$, where $\Omega$ is the Earth's rotation rate, and $\theta$ is the latitude. ($f$ can be approximated to be zero if the excited GWs are expected to have periods much smaller than a few hours.) Then the model speed of sound is $c_s = \sqrt{\gamma g \mathcal{H}} = 302$ m/s. The ground-based zonal phase speed is $c_x = \omega_r/k = \lambda_x/\tau_r = 50$ m/s. We calculate the non-dimensional wave amplitude to be $u'/(c_x - \overline{U}) \simeq 1$; this verifies that the waves are breaking (or saturated) at this altitude (Lindzen, 1981). Because the waves are eastward-propagating, they create an eastward zonal body force upon breaking. We parameterize this zonal body force as a Gaussian in space,

$$F_x(\mathbf{x}) = u_0 \exp\left( -\frac{(x - x_0)^2}{2\sigma_x^2} - \frac{(y - y_0)^2}{2\sigma_y^2} - \frac{(z - z_0)^2}{2\sigma_z^2} \right), \tag{5}$$

where $\mathbf{x}_0 = (x_0, y_0, z_0)$ is the center, $\sigma_x$, $\sigma_y$, and $\sigma_z$ are the Gaussian half-widths in the $x$, $y$, and $z$ directions, respectively, and $u_0$ is the amplitude (in m/s). The full widths and depths of the body force are $\mathcal{D}_x = 4.5\sigma_x$, $\mathcal{D}_y = 4.5\sigma_y$, and $\mathcal{D}_z = 4.5\sigma_z$. We assume that the wave packet is localized in space, and so average over two wavelengths and wave

periods. Our modeled zonal body force then has a diameter of $\mathcal{D}_x = \mathcal{D}_y = 60$ km, a depth of $\mathcal{D}_z = 30$ km, and a duration of $\chi = 20$ min. The maximum value of $\mathcal{F}$ is $2/\chi$ from Eq. (1). Additionally, $\overline{u'w'^*} \simeq u'w'/2$ due to the $\cos^2$ averaging in time. (Averaging in time also averages in space). Since the maximum value of $F_x$ is twice this average, we estimate $u_0$ to be:

$$u_0 = max(F_x) \sim \frac{u'w'\chi}{2\mathcal{H}}. \tag{6}$$

For this example, we estimate an amplitude of $u_0 \sim 70$ m/s from this wave packet, where we have assumed $\mathcal{H} \simeq 7$ km. This yields a maximum force amplitude of $2u_0/\chi = 0.1$ m/s$^2$.

Fig. 1 shows the Boussinesq and compressible zonal velocity perturbation spectra excited by this body force,

$$\sqrt{k^2\ (2|\overline{\widetilde{u}'\widetilde{u}'^*}|\ \Delta k\ \Delta l\ \Delta m)}, \qquad \sqrt{k^2\ (2|\overline{\widetilde{\xi}\widetilde{\xi}^*}|\ \Delta k\ \Delta l\ \Delta m)}, \tag{7}$$

respectively (see Eq. (36) of VF09). Note that in this paper, all of the Boussinesq solutions are calculated using the solutions in VF01. We see that the spectra are nearly the same for $\lambda_z < 50$ km. For $\lambda_z > 50$ km, the solutions are quite different; in particular, for horizontal wavelengths of $100 < \lambda_H < 1000$ km and intrinsic phase velocities of $c_{IH} \gtrsim 200$ m/s, the compressible amplitudes are significantly larger than the Boussinesq amplitudes. Here, $c_{IH} = \omega_{Ir}/k_H$, where

$$\omega_{Ir} = \omega_r - (k\overline{U} + l\overline{V}) \tag{8}$$

is the intrinsic frequency, $\tau_{Ir} = 2\pi/\omega_{Ir}$ is the intrinsic period, $k_H = \sqrt{k^2 + l^2}$, and $k_H = 2\pi/\lambda_H$ is the horizontal wavenumber. These GWs may be important for creating larger-scale thermospheric body forces, creating significant variability in the thermosphere (e.g., Oliver *et al.*, 1997; Djuth *et al.*, 2004), and/or for seeding ionospheric plasma bubbles (e.g., Makela *et al.*, 2010). From Fig. 1b, GWs with $\lambda_H = 100$ to 2000 km and $\lambda_z$ up to

400 km are excited by this force. The spectrum peaks at $\lambda_H = 100 - 400$ km, $\lambda_z = 25$ to 100 km, and vertical group velocities of $c_{gz} \sim 15 - 35$ m/s.

For select values of $\lambda_H$, we also plot the values of $\lambda_z$ where the GWs dissipating from kinematic viscosity and thermal diffusivity have maximum momentum fluxes (turquoise dots). Here, we use the analytic "quenching" formula for $m$ derived previously (Eqs. (14)-(15) in V07). We set $N_B = 1.9 \times 10^{-2}$ rad/s, $\mathcal{H} = 17$ km, and $\nu = 1 \times 10^4$ m$^2$/s, which are the typical of values at $z = 150$ km (VL09). Those GWs far below an imaginary line connecting these dots dissipate below this altitude. However, those GWs above this imaginary line propagate above this altitude. We also display the GWs that have maximum momentum fluxes at $z = 250$ km using the same quenching formula (red dots). Here, we set $N_B = 1.3 \times 10^{-2}$ rad/s, $\mathcal{H} = 35$ km, and $\nu = 5 \times 10^5$ m$^2$/s, which are typical of the values at $z = 250$ km (VL09). Only those GWs above these dots (i.e., with $\lambda_z \gtrsim 200$ km and intrinsic phase speeds of $c_{IH} \gtrsim 250$ m/s) can propagate to $z \simeq 250$ km. Using $c_{IH} = \lambda_H / \tau_{Ir}$, the condition for GWs with $\tau_{Ir} = 30$ and 60 min is that they have $\lambda_H \geq 450$ km and $\lambda_H \geq 900$ km, respectively.

Fig. 2 shows the combined GW and AW density perturbations, $\rho'/\overline{\rho}$, at $z = 150$ km excited by the same zonal body force as in Fig. 1b. A few minutes after the force begins, AWs are observed propagating away from the force in the $\pm x$ directions. (These waves are not well-resolved here). The density perturbation amplitudes are a few to 10%. The first visible GWs arrive at $t \sim 20$ min, and are still arriving after 2 hrs. The GW density perturbations are of order a few to 10%. Note that the GWs form concentric rings around the center of the forcing in this zero-wind, zero-viscosity example, and are asymmetric about $x = x_0$. The rings appear to expand outward in time; this is not the correct interpretation, however, because each image shows different GWs. Instead, as time progresses, GWs with larger periods (and smaller vertical group velocities, $c_{gz} \equiv \partial \omega_{Ir} / \partial m$) reach this altitude. At $t \sim 30$ min, the secondary GWs from the peak of

the GW spectrum in Fig. 1b arrive, with $c_{gz} \sim 35$ m/s and $\lambda_H \sim 100 - 300$ km. At $t = 90$ and 120 min, the GWs have $c_{gz} \sim 10$ m/s and larger horizontal wavelengths of $\lambda_H \sim 400-$ a few thousand km. Since dissipation is not included in the compressible (or Boussinesq) solutions, it is possible that some of the GWs visible in Fig. 2 would have dissipated below this altitude. This is not a major concern for $t \leq 120$ min, however, because these GWs have $c_{gz} > 5$ m/s, $\lambda_H > 100$ km, and $\lambda_z > 50$ km, and therefore dissipate at $z \geq 150$ km (see the turquoise dots in Fig. 1b).

*2. Geostrophic adjustment of the jet stream in the tropopause*

Geostrophic adjustment in the troposphere occurs when the jet stream changes direction or speed locally due to regional or continental changes in the geostrophic balance. Nicolls *et al.*(2010) observed approximately southward-moving inertial GWs over Poker Flat ISR (PFISR) on 23 April 2008 with $\lambda_H \sim 700 - 1600$ km, ground-based periods of $\tau_r \sim 9-13$ hr, $c_H \sim 10$ m/s, and $\lambda_z \sim 5$ km. Detailed analysis of the winds at $z \sim 60-80$ km showed that the waves likely had horizontal wavelengths of $\lambda_H \sim 700-1000$ km prior to entering the region above PFISR. (The region above PFISR had a southward wind component during the first 4-6 hrs of observations which was likely due to the dissipation of these waves. This meridional wind gradient likely increased the observed horizontal wavelengths for the first few hours of observations.) These waves may have been excited by a geostrophic adjustment of the jet stream in northern Russia ∼5 days earlier. This adjustment included both zonal and meridional acceleration components. However, because horizontal body forces do not excite waves with significant amplitudes perpendicular to their force direction (V03), we only model the meridional acceleration here. We model this geostrophic adjustment as a Gaussian meridional body force:

$$F_y(\mathbf{x}) = v_0 \exp\left(-\frac{(x-x_0)^2}{2\sigma_x^2} - \frac{(y-y_0)^2}{2\sigma_y^2} - \frac{(z-z_0)^2}{2\sigma_z^2}\right), \tag{9}$$

where $v_0$ is the amplitude (in m/s). The jet stream was maximum at $z = 9$ km; therefore,

we locate this body force at $z_0 = 9$ km. 12-hourly balloon sounding data showed the adjustment to have a width of 500 km and a depth of 5 km. Therefore, we set $\mathcal{D}_x = \mathcal{D}_y = 500$ km and $\mathcal{D}_z = 5$ km. This data also showed that the meridional wind increased by $\sim +25$ m/s within the 12 hours between the soundings; thus, $\chi \leq 12$ hours. As shown in V03, the mean wind created by a horizontal body force with similar $x$ and $y$ extents equals $v_0$ for any $\chi$. Therefore, we set the force amplitude to be $v_0 = 25$ m/s. We find that setting $\chi = 12$ hrs results in GW amplitudes that are too small at the PFISR observation altitudes. Therefore, we set $\chi = 6$ hr here, as this gives good agreement with the data, and is consistent with jet stream adjustment time scales. We also set $\mathcal{H} = 7$ km, $N_B = 0.02$ rad/s, $\gamma = 1.4$, $\mathrm{X_{MW}} = 30$, $g = 9.5$ m/s$^2$, $\overline{T} = 235$ K, and $f = 1.4 \times 10^{-4}$ rad/s (i.e., $\theta = 75^{\mathrm{o}}$N).

Fig. 3 shows the Boussinesq and compressible meridional velocity spectra which result from this body force. Here, we show the meridional velocity perturbation spectra:

$$\sqrt{l^2\ (2|\overline{\widetilde{v}'\widetilde{v}'^*}|\ \Delta k\ \Delta l\ \Delta m)}, \qquad \sqrt{l^2\ (2|\overline{\widetilde{\sigma}\widetilde{\sigma}^*}|\ \Delta k\ \Delta l\ \Delta m)}. \tag{10}$$

We see that the spectra are nearly identical. This is because the force is much shallower than $\mathcal{H}$. Some of these inertial waves have similar characteristics to those observed by Nicolls *et al.*(2010). In particular, those waves with $\lambda_H \sim 700 - 1000$ km and $\lambda_z \sim 5$ km have intrinsic horizontal phase speeds of $c_{IH} = 25$ m/s. Because $\overline{V} \sim 15$ m/s at the estimated excitation time and location, this yields a ground-based phase speed of $c_y \simeq 10$ m/s for the northward waves over Russia (which propagate southward after crossing the north pole), in agreement with the measured value.

Fig. 4 shows the GW zonal and meridional velocity perturbations, $u'$ and $v'$, excited by this body force at $t = 24$, 36, 48, and 60 hours. Note that $x = x_0$, $y = y_0 + 2550$ km, and $z = 35$ km is halfway between the jet stream maximum and the lowest observation altitude of $z = 60$ km. GWs are clearly visible. We note the coherency of the oscillations

with altitude for a single-location observer, even though many GWs are observed in each plot, since these waves propagate nearly horizontally. At early times, the GWs have larger $\lambda_H$ and $\lambda_z$, while at later times the GWs have smaller $\lambda_H$ and $\lambda_z$. Let us look at $x = x_0$, $y - y_0 = 2500$ km, and $z = 35$ km. At $t = 24$ hr, $\lambda_H \sim 1300$ km and $\lambda_z \sim 12$ km, while at $t = 36$ hr, $\lambda_H \sim 850$ km and $\lambda_z \sim 8$ km. Thus, $\lambda_H$ decreases by 40% in 12 hours. This decrease occurs because the vertical group velocity is smaller for a GW with the same $\omega_r$ but with a smaller $\lambda_H$, since GWs with the same $\omega_r$ propagate to the same location and altitude (for a windless, constant $\overline{T}$ atmosphere). Note that the horizontal wind amplitudes of the GW packet at $z = 35$ km, $t = 2$ days, and $y - y_0 \sim 2500 - 2700$ km are as large as 0.3 m/s. Because this wave's amplitude increases by $\exp(\Delta z/2\mathcal{H})$, its horizontal wind velocity is estimated to be $\sim 1.9$ m/s at $z = 61$ km, $t \sim 4$ days, and $y - y_0 \sim 5000 - 5500$ km. This value agrees with the measured value at this altitude (Nicolls *et al.*, 2010). (Note that because the southward wind increases near PFISR due to wave breaking, the transit time for this packet to reach the observed altitude is expected to be somewhat longer than 4 days.)

The results shown in Fig. 4 are linear, and therefore do not include wave saturation. However, only Fig. 4a shows $u'$ and $v'$ growing exponentially with altitude; the other panels show $u'$ and $v'$ constant or decreasing with altitude. This variation with altitude for non-saturating waves can be explained as follows. Because these GWs are nearly horizontally propagating, with approximately one wave per vertical interval equal to $\lambda_z$ (along the $z$-axis), we are seeing many GWs over this 40 km altitude range from $z = 20$ to 60 km. Therefore, the variation of the wave amplitudes with altitude are due entirely to the amplitude variations of the waves within the GW spectrum. Therefore, when one is viewing low-frequency waves as a function of altitude, one must be careful not to interpret the constancy (or decrease) of $u'$ and $v'$ with altitude as a definitive indication of wave saturation when the altitude range encompasses many different waves. Indeed, Nicolls

263 *et al.*(2010) showed that these waves saturated via calculating the non-dimensional wave
264 amplitudes.

265 *3. Thermospheric body force from the dissipation/breaking of GWs*

266 As has been shown previously, the dissipation and/or breaking of GWs in the ther-
267 mosphere creates localized, interval, horizontal, thermospheric body forces (VF04; VF06;
268 VL09; Vadas and Crowley, 2009, hereafter VC09). The mean winds and accelerations
269 caused by these forces have been observed at high latitudes (Vadas and Nicolls, 2008,
270 2009). These body forces excite secondary GWs. VF06 estimated the peak of the sec-
271 ondary GW spectrum to occur at $\lambda_H \sim$ twice the horizontal width and $\lambda_z \sim 1-2$ times
272 the depth of the forcing. VF04, VF06 and VL09 calculated the thermospheric body
273 forces created by single convective plumes. They found the horizontal extents of the
274 body forces to be at least 400 km. This led to the estimate that secondary GWs would
275 have $\lambda_H = 200 - 5000$ km, with a peak at $\lambda_H \sim 800$ km. VL09 found that large scale
276 GWs with $\lambda_H \sim 2100$ km are indeed excited by thermospheric body forces; however, this
277 study was unable to resolve GWs with $\lambda_H < 2000$ km. A recent study examined the body
278 forces created from multiple plumes and clusters (VC09). They found that constructive
279 and destructive wave interference create thermospheric body forces with horizontal vari-
280 ability on scales of order $100-400$ km. This led to a revised estimate that the secondary
281 GWs would have $\lambda_H > 100$ km, with a peak at $\lambda_H \sim$ a few hundred km. However, no
282 study to date has calculated the secondary GW spectra from thermospheric body forces
283 for $\lambda_H < 2000$ km. We do so now for a few simple cases, in order to understand the
284 basic spectra which result. Work is in progress to calculate the secondary GW spectra
285 for more realistic thermospheric body forces.

286 Although a thermospheric body force has zonal and meridional components in general,
287 $(F_x\hat{i} + F_y\hat{j})\mathcal{F}$ (VL09), we simulate a meridional body force here for simplicity. Using

Eq. (9), we first simulate an extremely shallow meridional body force at a midlatitude location with medium-scale horizontal variability: $\mathcal{D}_x = \mathcal{D}_y = 100$ km, $\mathcal{D}_z = 10$ km, and $f = 1 \times 10^{-4}$ rad/s (i.e., midlatitude). Because body force altitudes range from 110 to 190 km (VC09), we choose an intermediate value of $z_0 = 150$ km. We also choose $\mathcal{H} = 23$ km, $N_B = 0.012$ rad/s (i.e., a buoyancy period of $\tau_b = 2\pi/N_B \simeq 9$ min), $\gamma = 1.55$, $\mathrm{X_{MW}} = 20$, $g = 9.4$ m/s$^2$, and $\overline{T} = 515$ K, which are typical of the values at $z \sim 190$ km, in order that we may estimate the density and velocity perturbations at $z \sim 240$ km from these isothermal solutions. VC09 found that the temporal variability of the body forces is $\leq 15$ min; therefore, we set $\chi = 15$ min. Finally, VL09 and VC09 found that the maximum body force amplitudes range from 0.5 to 1 m/s$^2$ (including wave saturation). Therefore, we choose an amplitude of 0.5 m/s$^2$ here. Since the maximum body force amplitude is

$$2v_0/\chi, \tag{11}$$

we obtain $v_0 = 225$ m/s.

Fig. 5a-b shows the Boussinesq and compressible meridional velocity perturbation spectra for the excited GWs (using Eq. (10)). We see that the Boussinesq and compressible solutions are nearly identical. This is because $\mathcal{D}_z < \mathcal{H}$ for this unrealistically shallow body force. Although the spectrum peaks at $\lambda_H \lesssim 150$ km, secondary GWs with $\lambda_H$ up to 1000 km are also excited. Part of the GW source spectrum is above the turquoise dots; these GWs can propagate at least some distance above $z = 150$ km. The red dots are not visible, because none of these GWs are expected to have maximum momentum fluxes at or above $z \sim 250$ km.

Fig. 5c-d shows the Boussinesq and compressible GW spectra from the same body force as in a-b, but with $\mathcal{D}_z = 40$ km. This shallow force may be more typical of thermospheric body forces from convective overshoot during extreme solar minimum. For this

force, the Boussinesq and compressible solutions differ significantly because $\mathcal{D}_z \gg \mathcal{H}$. In particular, the tails of the spectra behave differently, with $\lambda_z > 150$ km and $\lambda_H < 600$ km GWs having much larger amplitudes for the compressible solutions. Therefore, compressibility must be accounted for when calculating the excited secondary GW spectrum from realistic thermospheric body forces. All of the excited GWs are above the turquoise dots. Therefore, this entire GW spectrum is likely excited by this force. Only those GWs with $\lambda_z \gtrsim 150$ km and $c_{IH} \gtrsim 250$ m/s are expected to have maximum momentum fluxes at or above $z \simeq 250$ km, however. These tend to be GWs with $200 \lesssim \lambda_H \lesssim 600$ km.

Fig. 5e-f shows the Boussinesq and compressible GW spectra from the same body force as in a-b, but with $\mathcal{D}_z = 100$ km. This deep force may be more typical of thermospheric body forces when the thermosphere is warm ($\overline{T} \sim 1000$ K) (VL09; VC09). For this force, the Boussinesq and compressible solutions differ dramatically. In particular, the solutions peak at different vertical scales, with the compressible amplitudes being typically larger (sometimes much larger) than the Boussinesq amplitudes for $\lambda_z > 200$ km. All of the GW source spectrum is above the turquoise dots. Therefore, this entire GW spectrum is excited by this force. Since most of the excited GWs have $\lambda_z \gtrsim 150$ km and $c_{IH} \gtrsim 250$ m/s for this deep source, most are expected to propagate above $z \simeq 250$ km. These include GWs with $100 \lesssim \lambda_H \lesssim 1500$ km.

Comparing Fig. 5d and f, we see that the deep thermospheric body force excites GWs with much larger $\lambda_H$ and $\lambda_z$ than the shallow body force; the shallow body force excites GWs which peak at $\lambda_H = 100 - 400$ km, $\lambda_z = 50 - 125$ km, and $\tau_{Ir} \sim 20 - 40$ min, while the deep body force excites GWs which peak at $\lambda_H = 100 - 800$ km, $\lambda_z = 100 - 600$ km, and $\tau_{Ir} \sim 15 - 40$ min. This difference is extremely important, because GWs with larger $\lambda_z$ and $\omega_{Ir}$ can penetrate to much higher altitudes in the thermosphere prior to dissipating (V07).

We point out that a strong local-time dependence has been observed for traveling

ionospheric disturbances (TIDs) detected at the bottomside of the F layer (MacDougall *et al.*, 2009). In particular, during spring and fall (the summer data was incomplete), they observed TIDs with 1) horizontal phase speeds of $\sim$ 90 to 250 m/s during the morning and early afternoon hours, and 2) horizontal phase speeds of $\sim$ 100 to 500 m/s during the afternoon through midnight hours. This is the expected local time trend for deep convection, since solar heating evaporates water during the day, creating afternoon and evening thunderstorms. If these TIDs can be associated with GWs, then those waves with horizontal phase speeds of $c_H \gtrsim 280$ m/s could not have been generated in the lower atmosphere. We postulate that many of these fast waves (and waves with speeds down to $\sim$ 100 m/s) could have been secondary GWs excited by thermospheric body forces created by deep convective overshoot in afternoon and evening thunderstorms. Indeed, VC09 showed this to be the case in their study.

Rows 1 and 2 of Fig. 6 show the combined GW and AW density perturbations, $\rho'/\overline{\rho}$, at $z = 240$ km excited by the same thermospheric body forces as for Fig. 5d and 5f, respectively. Concentric rings of GWs centered on the forces are clearly visible, with meridional asymmetry about $y = y_0$. Density perturbation amplitudes are up to 3%. The rings appear to expand outwards in time; as discussed before, this is an illusion, because each image contains different GWs with different parameters. Instead, this effect is caused by GWs with larger periods reaching this altitude at later times. At $t \sim 20$ and 30 min, the shallow and deep forcing solutions look similar. The secondary GWs seen at $t \sim 30$ min are at or near the peak of the wave spectra, with $\lambda_H \sim 100 - 600$ km and $c_{gz} \sim 50$ m/s (see Fig. 5). At $t = 60$ and 90 min, however, the shallow and deep forcing solutions look quite different. In particular, the GWs from the shallow force have $\lambda_H \leq 300$ km and $r \leq 600$ km, while the GWs from the deep force have $300 \leq \lambda_H \leq 3000$ km and $r \leq 3000$ km, where $r = \sqrt{(x - x_0)^2 + (y - y_0)^2}$ is the radius. When the winds

are zero, a GW's intrinsic frequency can be approximated as (Kundu, 1990)

$$\omega_{Ir} \sim N_B \cos\theta, \tag{12}$$

where $\theta$ is the angle of the GW's ray path from the zenith (vertical), and $\tan\theta = r/|z-z_0|$. Using $|z - z_0| = 90$ km, these radial locations imply intrinsic periods of $\tau_{Ir} \leq 60$ min and $\tau_{Ir} \leq 300$ min for the shallow and deep forces, respectively. The differences in these solutions arise from the differences in the excited secondary wave spectra. The vertical group velocities of the GWs reaching this altitude at $t = 60$ and 90 min are $c_{gz} \sim 25$ and 15 m/s, respectively. From Fig. 5d, GWs excited from the shallow force with $c_{gz} \sim 15$ m/s have $\lambda_H \gtrsim 150$ km, with the largest relative amplitudes (0.9) having $\lambda_H \sim 150$ km. Those excited GWs with $\lambda_H \simeq 1000$ km and $c_{gz} \sim 15$ m/s have amplitudes $\lesssim 0.3$. On the other hand, GWs excited from the deep force with $c_{gz} \sim 15$ m/s have $\lambda_H \sim 100-200$ km and $\lambda_H \geq 1000$ km, with the latter waves having the largest amplitudes ($\sim 0.3$). Therefore, the difference in the solutions at $t = 60$ and 90 min occurs because the shallow force excites GWs with $\lambda_H \sim 150$ km that have relatively larger amplitudes than the $\lambda_H > 1000$ km GWs (which have comparable amplitudes with the $\lambda_H > 1000$ km GWs excited by the deep force).

As mentionned previously, dissipation is not included in the compressible solutions. Dissipation will affect those GWs with $\lambda_z < 150$ km and $c_{gz} < 30$ m/s at this altitude, because they would have dissipated below $z = 240$ km (see Fig. 5d and 5f). These GWs arrive at $z \simeq 240$ km at $t \gtrsim 50$ min. Therefore, some of the waves in Fig. 6 at $t = 60$ min, and especially at $t = 90$ min, might dissipate below this altitude if dissipation were included.

Fig. 7 shows the horizontal and vertical velocity perturbations at $t = 30$ min at $z = 240$ km. The GWs have $\lambda_H \sim 200 - 300$ km, with meridional and vertical velocity perturbations of 13 and 10 m/s, respectively. Because $r \sim 200$ km, we estimate $\tau_{Ir} \sim$

20 min using Eq. (12). Note that these parameters are typical of the secondary GWs identified in VC09.

We postulated in VL09 that secondary GWs were likely the cause of the density perturbations observed by the CHAMP satellite at $z \sim 400$ km. We now estimate the density perturbations at $z \sim 400$ km for the peak secondary GWs excited from the deep thermospheric body force with $\lambda_H \sim 200-600$ km and $\tau_{Ir} \sim 15-30$ min. (Some of these waves are seen in Fig. 6f at $t = 30$ min.) Assuming $\overline{T} = 1000$ K and launch altitudes of $z_i = 150 - 180$ km, Fig. 6c-d in V07 shows that the GWs with $\lambda_H \sim 200 - 600$ km have maximum momentum fluxes at $z \sim 250-325$ km. Above these altitudes, the amplitudes of those GWs with $\lambda_z \gtrsim 200$ km are approximately constant because $\lambda_z$ is so large. From Fig. 6f, $\rho'/\overline{\rho} \sim 1 - 2\%$ for these GWs at $z = 240$ km. Using an average density scale height from $z \sim 240$ to 300 km of $\mathcal{H} \sim 35$ km, we estimate a maximum value (for the GWs with the largest $\lambda_z$) of $\rho'/\overline{\rho} \sim 1.5\% \times \exp[(275 - 240)/70] \sim 2.5\%$ at $z \sim 400$ km. We compare this result with the density perturbations measured by CHAMP at equatorial latitudes for low $Kp$, where convective overshoot is the most likely source of thermospheric body forces; Fig. 4 of Bruinsma and Forbes (2008) report $\rho'/\overline{\rho} \sim 1 - 2\%$. Therefore, our results agree well with the observed values.

## 4. Wave Responses to Vertical Body Forces

A vertical body force can be used to model the excitation of GWs from the overshooting of the tropopause by the "envelope" of a deep convective plume. The spectrum of excited GWs includes GWs with $20 < \lambda_H < 350$ km (Vadas *et al.*, 2009). In order to include ground reflection, we model a single convective plume as an upward-moving vertical body force centered at $(x, y, z) = (x_0, y_0, z_0)$ plus an identical and simultaneous downward-moving "image" vertical body force centered below the Earth's surface at $(x, y, z) = (x_0, y_0, -z_0)$ (VF09). This image body force pushes air downwards at the same

time as the body force above the ground pushes air upwards. Because the downward-propagating GWs and AWs from the above-ground body force reach $z = 0$ at the same time as the upward-propagating GWs and AWs from the image force, it appears that those downward-propagating GWs and AWs "reflect" upwards at the Earth's surface. This configuration also automatically sets the vertical velocity to zero at the ground (i.e., at $z = 0$). This configuration is represented mathematically as

$$F_z(\mathbf{x}) = F_0 \exp\left(-\frac{(x-x_0)^2}{2\sigma_x^2} - \frac{(y-y_0)^2}{2\sigma_y^2}\right) \left[\exp\left(-\frac{(z-z_0)^2}{2\sigma_z^2}\right) - \mathrm{e}^{(-z_0/\mathcal{H})} \exp\left(-\frac{(z+z_0)^2}{2\sigma_z^2}\right)\right]. \quad (13)$$

Here, we multiply the image vertical body force amplitude by $\mathrm{e}^{(-z_0/\mathcal{H})}$ (within the square brackets) for the compressible solutions; for the Boussinesq solutions, we set this factor equal to one (VF09). This factor is needed for the compressible solutions to ensure that the amplitudes of the downgoing waves from the body force equal the amplitudes of the upgoing waves from the image force at the ground.

We model a single convective plume with a diameter of $\mathcal{D}_x = \mathcal{D}_y = 15$ km, a depth of $\mathcal{D}_z = 10$ km, and a duration of $\chi = 10$ min. We also choose a tropopause altitude of $z_{\mathrm{trop}} = 14$ km and an overshoot depth of 1 km. The center of the body force is then located at $z_0 = 10$ km. We also choose $F_0 = 530$ m/s, as this results in a maximum plume updraft velocity of $w_{\mathrm{pl}} = 35$ m/s. These model values are typical of convective overshoot in thunderstorms (e.g., Vadas *et al.*, 2009; VL09). Fig. 8 shows the Boussinesq and compressible GW spectra excited from this plume. Note that a) is nearly identical to Fig. 3 in VL09. For $\lambda_H < 100$ km and $\lambda_z < 50$ km, the Boussinesq and compressible solutions are nearly identical. For $\lambda_z > 100$ km and $100 < \lambda_H < 150$ km, the compressible amplitudes are $\sim 2$ times larger than the Boussinesq amplitudes. For $\lambda_z > 50$ km and $\lambda_H > 200$ km, the Boussinesq amplitudes are $\sim 2-3$ times larger than the compressible amplitudes. While more than one-half of the GWs in this envelope spectrum survive to

$z \sim 150$ km (turquoise dots), few can propagate far above $z \sim 250$ km (red dots).

Fig. 9 shows the GW and AW zonal and vertical velocity perturbations at $t = 15$ min and $y = y_0$ calculated from the compressible solutions. Here, we multiply the amplitudes by $\mathrm{e}^{-(z-z_0)/2\mathcal{H}}$ in order to view the characteristics of the solutions over a large altitude range. a)-d) show the GW and AW solutions for a typical convective plume duration of $\chi = 10$ min. e)-h) show the GW and AW solutions for an unrealistically short duration of $\chi = 1$ min. All solutions show waves propagating away from the centers of the force and image force, with reflection occurring at $z = 0$. Additionally, the GWs (AWs) move relatively slowly (rapidly) away from the body forces, as expected. Finally, all solutions display the required zonal symmetry/asymmetry and zero vertical velocity at $z = 0$.

For the plume with $\chi = 10$ min, the GW zonal and vertical velocity amplitudes are 2000 and 800 times larger, respectively, than the corresponding AW amplitudes at the same time. This is partly due to the cutoff factor in the AW solutions (Vadas, 2010)

$$\frac{\hat{a}^2}{\chi\omega_{AW}(\hat{a}^2 - \omega_{AW}^2)}, \tag{14}$$

where $\omega_{AW}$ is the AW frequency. This reduces the AW amplitudes by $\sim (1/2\pi)(\hat{a}/\omega_{AW})^3 \sim 1/400$ in this case. The characteristic time scale of this plume is (VF01)

$$\tau_c = \tau_b\sqrt{(\mathcal{D}_x/\mathcal{D}_z)^2 + 1} \tag{15}$$

for $\mathcal{D}_x = \mathcal{D}_y$; therefore $\tau_c = 9$ min for this plume. Because $\chi \simeq \tau_c$, there is little cut-off of the high-frequency portion of the GW spectrum in this case. Therefore, we expect the amplitudes of the excited GWs to be $\sim 400$ times larger than the amplitudes of the excited AWs. Additionally, the AW perturbation amplitudes will also be smaller at a fixed time because of geometric attenuation, which causes a wave's amplitude to decrease as it propagates away from a source. This occurs because the AWs have much faster propagation speeds than the GWs.

As seen in e)-h), the AW perturbation amplitudes increase significantly when the plume duration is shortened to 1 min. In this case, the GW zonal and vertical velocity amplitudes are only 30 and 80 times larger, respectively, than the corresponding AW amplitudes. Most of this difference is due to geometric attenuation. Although instructive, e)-h) does not represent realistic solutions because $\chi = 1$ min is too small. Such short duration variability is more characteristic of the smaller-scale updrafts that occur within a convective plume envelope; these smaller-scale variabilities are likely associated with waves having small horizontal wavelengths of $\lambda_H \simeq 5 - 10$ km (Lane *et al.*, 2001; 2003).

Fig. 10 shows the combined GW and AW temperature perturbations at $z = 90$ km for the same convective plume from Fig. 8b. The upper row shows mainly the AWs, while the lower row shows mainly the GWs. Because of the cylindrical symmetry of the forcing, both AWs and GWs propagate as concentric rings from the center of the forcing. However, due to wave dispersion, the GW images have many bands of rings. Temperature perturbations are 2-7% for the AWs and 2-23% for the GWs. By $t = 10$ min, the AWs are virtually gone, having propagated above 90 km. At $t = 80$ min, the GWs are still visible with large amplitudes

As noted previously, the larger $\lambda_H$ GWs propagate to the mesopause prior to the smaller $\lambda_H$ GWs for radii of $r \lesssim 500$ km (i.e., Vadas *et al.*, 2009). In Fig. 10e, GWs with $\lambda_H \sim 300$ km are present at $r \sim 300$ km and $t = 20$ min, with a small amplitude of $T'/\overline{T} \sim 2\%$. These GWs have very fast horizontal phase speeds of $c_H \sim r/\Delta t \sim 250$ m/s, where $r \sim 300$ km and $\Delta t = 20$ min. Since $c_H = \lambda_H/\tau_r$, this implies an intrinsic period for these GWs of $\tau_{Ir} = \tau_r \sim \lambda_H/c_H \sim 20$ min. Additionally, $\lambda_z \sim \lambda_H \tau_b/\tau_{Ir} \sim 80$ km. Therefore, these GWs may be quite important for penetrating deeply into the thermosphere (V07). At $t = 40$ min (Fig. 10f), GWs with $\lambda_H \sim 150$ km are observed at $r \sim 250$ km with a large amplitude of $T'/\overline{T} \sim 20\%$. These waves have fast horizontal phase speeds of $c_H \sim 100$ m/s. At $t = 80$ min (Fig. 10h), there are many smaller-scale

GWs near the center of the image with $\lambda_H \sim 50 - 150$ km. However, larger-scale GWs with $\lambda_H \sim 300$ km can also be observed at this time at large radii of $r \simeq 800 - 1000$ km. These waves have fast horizontal phase speeds of $c_H \sim 190$ m/s, and intrinsic periods of $\tau_{Ir} = \tau_r \sim \lambda_H / c_H \sim 25$ min. Additionally, $\lambda_z \sim \lambda_H \tau_b / \tau_{Ir} \sim 60$ km. Therefore, these GWs may also be important in the thermosphere, although they cannot propagate as high as the $\lambda_H \sim 300$ km GWs present at $t = 20$ min and $r = 300$ km (if the winds are zero) (V07).

## 5. Wave Responses to Heatings

A general heating can be used to describe the input of energy from the aurora into the thermosphere. We model this heating as a simple Gaussian function

$$J(\mathbf{x}) \;=\; J_0 \exp\left( -\frac{(x-x_0)^2}{2\sigma_x^2} - \frac{(y-y_0)^2}{2\sigma_y^2} - \frac{(z-z_0)^2}{2\sigma_z^2} \right), \tag{16}$$

where $J_0$ is the amplitude in m/s$^2$. Note that auroral heatings tend to be arc-shaped instead. Additionally, the aurora moves rapidly in time. However, we use this simple heating model in order to understand the basic properties of the excited GWs and AWs.

We first model a localized heating at $z_0 = 140$ km as a sphere with $\mathcal{D}_x = \mathcal{D}_y = \mathcal{D}_z = 10$ km, $\chi = 1$ min, and $J_0 = 20$ m/s$^2$. We also choose $\mathcal{H} = 23$ km, $N_B = 0.012$ rad/s, $\gamma = 1.55$, $\mathrm{X_{MW}} = 20$, $g = 9.4$ m/s$^2$, $f = 1.4 \times 10^{-4}$ rad/s, and $\overline{T} = 515$ K, typical of the values at $z \sim 190$ km at a high latitude, in order that we may estimate the density and velocity perturbations at $z \sim 250$ km from these isothermal solutions. Fig. 11a-b shows the GW zonal velocity spectra excited by this heating from the Boussinesq and compressible solutions. We see that the solutions are nearly identical. This occurs because $\mathcal{D}_z < \mathcal{H}$. Since most of the excited GWs are above the turquoise dots, most of the excited GWs will propagate at least some distance from the heating. The red dots cannot be seen, because none of these waves have maximum momentum fluxes at or above $z \sim 250$ km (V07).

Fig. 11c-d shows the excited GW spectra excited from the same heating as in Fig. 11a-b, but with $\mathcal{D}_x = 100$ km, more representative of a realistic "line-shaped" auroral heating. The spectra are nearly identical because $\mathcal{D}_z < \mathcal{H}$. However, the excited GWs with $\lambda_H > 200$ km, $\lambda_z > 100$ km, and $c_H > 100$ m/s have much larger amplitudes than in Fig. 11a-b. This difference is very important, because these latter waves can propagate to much higher altitudes in the thermosphere (V07). Although the peak in Fig. 11d occurs at $100 < \lambda_H < 250$ km and $20 < \lambda_z < 200$ km, some of the GWs have $\lambda_H \sim 300$ to more than 1000 km. Since all of the excited GWs are above the turquoise dots, all of the excited GWs will propagate at least some distance above this source. Those GWs with $\lambda_z \gtrsim 150$ km and $c_H \gtrsim 200 - 300$ m/s have maximum momentum fluxes at or above $z \simeq 250$ km.

Fig. 12 shows the AW and GW density perturbations separately at $z = 250$ km from the same heating as in Fig. 11b. Because the AW speed is $c_s \sim 580$ m/s in this model, the minimum transit time for AWs from $z = 140$ to 250 km is $\sim 3 - 4$ min. Fig. 12a-d shows the AW responses at $t = 4$, 5, 6, and 8 min. The AWs form a single concentric ring around the center of the heating. This ring expands in time. Fig. 12e-h shows the GW responses at $t = 30$, 60, 90, and 120 min. The excited GWs also form concentric rings around the center of the heating; however, many frequencies are visible at the same time due to wave dispersion. At earlier (later) times, the GWs have larger (smaller) $\lambda_H$ for this high-frequency portion of the spectrum.

Fig. 13 shows the AW and GW vertical velocity perturbations separately at $z = 250$ km from a line-shaped heating at $z_0 = 140$ km with $\mathcal{D}_x = 400$ km and $\mathcal{D}_y = \mathcal{D}_z = 10$ km. All other parameters are as before. The excited AWs and GWs now form linear bands which propagate in the meridional direction away from this source. Although only single bands are visible for the AWs, there are multiple bands for the GWs because of wave dispersion. For the GWs, $\lambda_y \sim 200$ km at $t \simeq 30$ min, and is $\lambda_y \sim 40$ km at

$t \simeq 120$ min in this non-dissipative atmosphere. However, these latter waves are unlikely to propagate to this altitude because of viscous dissipation (V07). Ray tracing the source spectrum through realistic dissipation, winds, and temperatures needs to be performed to determine the solution more accurately at this altitude and time.

## 6. Conclusions

In this paper, we examined the solutions to 5 important body forcings and heatings in our neutral atmosphere. We calculated the Boussinesq and compressible GW solutions. We found that for forcings/heatings shallower than $\mathcal{H}$, these solutions are nearly identical. For forcings/heatings deeper than $\mathcal{H}$, the compressible amplitudes of the GWs with $\lambda_z \lesssim 2\pi\mathcal{H}$ are nearly identical to the Boussinesq amplitudes. However, for GWs with $\lambda_z \gtrsim 2\pi\mathcal{H}$, the solutions can differ substantially. In the lower atmosphere, the compressible solutions are necessary for describing the GW response for GWs with $\lambda_z \gtrsim 50$ km.

We modeled the breaking of eastward-propagating GWs with $\lambda_x = 30$ km and $\lambda_z = 15$ km near the mesopause as a zonal body force. The force excited GWs with $\lambda_H = 100$ to 2000 km and $\lambda_z = 30$ to 400 km. We found that the compressible amplitudes were much larger than the Boussinesq amplitudes for high-frequency GWs with $100 < \lambda_H < 1000$ km, $\lambda_z > 100$ km, and $c_H > 200$ m/s. At $z \sim 150$ km, the GWs form concentric rings around the center of the force, with $\rho'/\overline{\rho}$ as large as $\sim 10\%$. The AWs propagate zonally, and have $\rho'/\overline{\rho}$ as large as $\sim 10\%$ at $z \sim 150$ km.

We modeled a jet stream adjustment in northern Russia as a meridional body force. Because the depth of the forcing is much less than $\mathcal{H}$, the compressible and Boussinesq GW spectra were nearly identical. We found that the excited GWs have $\lambda_H \sim 300$ to thousands of km. This spectrum includes GWs with $\lambda_H \sim 700 - 1000$ km, $\lambda_z \sim 5$ km, and $c_{IH} = 25$ m/s which were observed at PFISR $\sim 5$ days later (Nicolls *et al.*, 2010). We also estimated the horizontal velocity perturbation to be 1.9 m/s at $z \sim 60$ km, in

reasonable agreement with the observations.

We modeled the dissipation and breaking of northward-propagating primary GWs in the thermosphere as meridional body forces. We found that the Boussinesq and compressible solutions are the same for unrealistically shallow forces. For realistic shallow and deep forces, however, the solutions differed significantly for $\lambda_z > 100$ km and $c_{IH} > 150$ m/s. When these forces are deep ($\mathcal{D}_z \sim 100$ km), they excite large-amplitude (peak) secondary GWs with significantly larger $\lambda_H$ and $\lambda_z$ than when the body forces are shallow ($\mathcal{D}_z \sim 40$ km). For example, the shallow body force excites GWs which peak at $\lambda_H = 100 - 400$ km, $\lambda_z = 50 - 125$ km, and $\tau_{Ir} \sim 20 - 40$ min, while the deep body force excites GWs which peak at $\lambda_H = 100 - 800$ km, $\lambda_z = 100 - 600$ km, and $\tau_{Ir} \sim 15 - 40$ min. Using the results from V07, we conclude that the secondary GWs excited by a deep thermospheric body force can penetrate deeper into the thermosphere prior to dissipating than a shallow force. We also found that the excited secondary GWs have $\rho'/\overline{\rho} = 1 - 3\%$ and $v', w' \sim 10 - 15$ m/s at $z \sim 240$ km. These are consistent with the values obtained in VL09. We also estimated $\rho'/\overline{\rho}$ as large as $\sim 2.5\%$ at $z \sim 400$ km. This value is consistent with CHAMP measurements (Bruinsma and Forbes, 2008).

We modeled the overshoot of a deep convective plume at the tropopause as a vertical body force plus an image force. We found that the compressible spectrum is quite different from the Boussinesq spectrum for $\lambda_H > 100$ km and $\lambda_z > 50$ km; the amplitudes are approximately twice as large for $100 < \lambda_H < 150$ km and $\lambda_z > 100$ km, but are approximately half as large for $\lambda_H > 200$ km and $\lambda_z > 50$ km. We identified the GWs at $z = 90$ km (in the $T'/\overline{T}$ images) which likely penetrate deeply into the thermosphere.

Finally, we modeled a line-shaped auroral heating in the thermosphere. We found that GWs with $\lambda_H = 100$ to 1000 km and $\lambda_z = 20$ to 200 km are excited. These waves have periods of 10 to 60 min and horizontal phase speeds of up to $\sim 350$ m/s. AWs are also excited with $\rho'/\overline{\rho}$ and $w'$ amplitudes similar to that of the GWs.

Because high-frequency GWs with $\lambda_H > 100$ km and $\lambda_z > 50$ km are important in the thermosphere via creating variability, are important for thermospheric dynamics via creating thermospheric body forces, and are potentially important for seeding plasma instabilities, it is important to calculate their amplitudes accurately. Since large differences between the compressible and Boussinesq solutions exists for these GWs, the compressible solutions are necessary for modeling the excitation of these large-$\lambda_z$, large-$c_{IH}$ GWs. In conclusion, the compressible solutions are necessary for modeling the excitation of GWs from wave breaking near the mesopause, thermospheric body forces, and convective plumes for atmospheric coupling studies. Additionally, the compressible solutions are needed for calculating the AW solutions, which can have large amplitudes when the temporal variability of the forcing/heating is $\chi \lesssim 10 - 20$ min.

**Acknowledgments** We would like to thank M.J. Nicolls for helpful suggestions. This research was supported by NSF grants ATM-0836195, and NASA contracts NNH07CC81C and NNH08CE12C.

## References


Alexander, M. J., J. R. Holton, and D. R. Durran, 1995: The gravity wave response above deep convection in a squall line simulation, *J. Atmos. Sci.*, **52**, 2212–2226.

Andreassen, Ø., P.Ø. Hvidsten, D.C. Fritts and S. Arendt, 1998: Vorticity dynamics in a breaking internal gravity wave. Part 1. Initial instability evolution, *J. Fluid Mech.*, **367**, 27–46.

Andrews, D. G., J. R. Holton, and C. B. Leovy, 1987: Middle atmosphere dynamics, Academic Press, Florida.

Beres, J.H., 2004: Gravity wave generation by a three-dimensional thermal forcing, *J. Atmos. Sci.*, **61**, 1805–1815.

Blumen, W., 1972: Geostrophic Adjustment, *Rev. Geophys. Space Phys.*, **10**, 485–528.

Bruinsma, S.L. and J.M. Forbes, 2008: Medium to large-scale density variability as observed by CHAMP, *Space Weath.*, **6**, S08002, doi:10.1029/2008SW000411.

Cowling, D. H., H. D. Webb, and K. C. Yeh, 1971: Group rays of internal gravity waves in a wind-stratified atmosphere, *J. Geophys. Res.*, **76**, 213–220.

Crowley, G, T.B. Jones, and J.R. Dudeney, 1987: Comparison of short period TID morphologies in Antarctica during geomagnetically quiet and active intervals, *J. Atmos. Terres. Phys.*, **49**, 1155–1162.

Dickinson, R. E., 1969: Propagators of atmospheric motions, 1. Excitation by point impulses, *Rev. Geophys.*, **7**, 483–538.

Djuth, F.T., M.P. Sulzer, S.A. Gonzales, J.D. Mathews, J.H. Elder, and R.L. Walterscheid, 2004: A continuum of gravity waves in the Arecibo thermosphere? , *Geophys. Res. Lett.*, **31**, 10.1029/2003GL019376.

Dunkerton, T. J., 1982: Stochastic parameterization of gravity wave stresses, *J. Atmos. Sci.*, **39**, 1711-1725.

Fritts, D. C., and Z. Luo, 1992: Gravity wave excitation by geostrophic adjustment of

627 the jet stream, Part I: Two-dimensional forcing, *J. Atmos. Sci.*, **49**, 681–697.
628 Fritts, D.C., S. Arendt, and Ø. Andreassen, 1998: Vorticity dynamics in a breaking inter-
629 nal gravity wave. Part 2. Vortex interactions and transition to turbulence, *J. Fluid Mech.*,
630 **367**, 47–65.
631 Fritts, D.C., S.L. Vadas, and Y. Yamada, 2002: An estimate of strong local body forc-
632 ing and gravity wave radiation based on OH airglow and meteor radar observations,
633 *Geophys. Res. Lett.*, **29(10)**, 1429, 10.1029/2001GL013753.
634 Fritts, D. C., and M. J. Alexander, 2003: Gravity wave dynamics and effects in the middle
635 atmosphere, *Rev. Geophys.*, **41**, 10.1029/2001RG000106.
636 Fritts, D. C., S. L. Vadas, K. Wan, and J. A. Werne, 2006: Mean and variable forcing of
637 the middle atmosphere by gravity waves, *J. Atmos. Solar Terres. Phys.*, **68**, 247–265.
638 Fritts, D. C. and S. L. Vadas, 2008: Gravity wave penetration into the thermosphere:
639 Sensitivity to solar cycle variations and mean winds, *Ann. Geophys.*, **26**, 3841-3861.
640 Fritts, D. C., S. L Vadas, D. M. Riggin, M. A. Abdu, I. S. Batista, H. Takahashi, A.
641 Medeiros, F. Kamalabadi, H.-L. Liu, B. J. Fejer, and M. J. Taylor, 2008b: Gravity
642 wave and tidal influences on equatorial spread F based on observations during the
643 Spread F Experiment (SpreadFEx), *Ann. Geophys.*, **26**, 3235–3252.
644 Garcia, R. R., 1987: On the mean meridional circulation of the middle atmosphere,
645 *J. Atmos. Sci.*, **44**, 3599–3609.
646 Hecht, J. H., 2004: Instability layers and airglow imaging, *Rev. Geophys.*, **42**, RG1001,
647 doi:10.1029/2003RG000131.
648 Hickey, M. P. and K. D. Cole, 1988 A Numerical Model for Gravity Wave Dissipation in
649 the Thermosphere, *J. Atmos. Terres. Phys.*, **50**, 689–697.
650 Hines, C.O. 1960: Internal atmospheric gravity waves at ionospheric heights, *Can. J. Phys.*,
651 **38**, 1441–1481.
652 Hines, C. O., and C. A. Reddy, 1967: On the propagation of atmospheric gravity waves

653 through regions of wind shear, *J. Geophys. Res.*, **72**, 1015–1034.

654 Hines, C. O., 1972: Momentum deposition by atmospheric waves, and its effects on ther-
655 mospheric circulation, *Space Res.*, **12**, 1157–1161.

656 Hocke, K., K. Schlegel, and G. Kirchengast, 1996: Phases and amplitudes of TIDs in the
657 high-latitude F-region observed by EISCAT, *J. Atmos. Terres. Phys.*, **58**, 245–255.

658 Hocke, K., and K. Schlegel, 1996: A review of atmospheric gravity waves and traveling
659 ionospheric disturbances: 1982 - 1995, *Ann. Geophys.*, **14**, 917–940.

660 Holton, J. R. and M. J. Alexander, 1999: Gravity waves in the mesosphere generated by
661 tropospheric convection, *Tellus*, **51A-B**, 45–58.

662 Holton, J. R., 1982: The role of gravity wave-induced drag and diffusion in the momentum
663 budget of the mesosphere, *J. Atmos. Sci.*, **39**, 791–799.

664 Holton, J. R., 1983: The influence of gravity wave breaking on the general circulation of
665 the middle atmosphere, *J. Atmos. Sci.*, **40**, 2497–2507.

666 Horinouchi, T., T. Nakamura, and J. Kosaka, 2002: Convectively generated mesoscale
667 gravity waves simulated throughout the middle atmosphere, *Geophys. Res. Lett.*, **29**,
668 10.1029/2002GL016069.

669 Kelley, M. C., 1989: The Earth's Ionosphere, Academic Press, San Diego, 487 pp.

670 Kundu, P., 1990: Fluid Dynamics, Academic Press, San Diego, 638 pp.

671 Lane, T. P., M. J. Reeder, and T. L. Clark, 2001: Numerical modeling of gravity waves
672 generated by deep tropical convection, *J. Atmos. Sci.*, **58**, 1249–1274.

673 Lane, T. P., R.D. Sharman, T.L. Clark, and H-M. Hsu, 2003: An Investigation of turbu-
674 lence generation mechanisms above deep convection, *J. Atmos. Sci.*, **60**, 1297–1321.

675 Lastovicka, J., 2006: Forcing of the ionosphere by waves from below, *J. Atmos. So-*
676 *lar Terres. Phys.*, **68**, 479–497.

677 F. Li, A. Z. Liu, G. R. Swenson, J. H. Hecht, and W. A. Robinson, 2005: Observa-
678 tions of gravity wave breakdown into ripples associated with dynamical instabilities,

679 *J. Geophys. Res.*, **110**, D09S11, doi:10.1029/2004JD004849.

680 Lindzen, R.S., 1981: Turbulence and stress owing to gravity wave and tidal breakdown,
681 *J. Geophys. Res.*, **86**, 9707-9714.

682 Luo, Z., and D. C. Fritts, 1993: Gravity wave excitation by geostrophic adjustment of
683 the jet stream, Part II: Three-dimensional forcing, *J. Atmos. Sci.*, **50**, 104–115.

684 MacDougall, J. W., G.Li and P. T.Jayachandran, 2009: Traveling ionospheric distur-
685 bances near London, Canada, *J. Atmos. Solar Terres. Phys.*, **71**, 2077-2084.

686 Makela, J.J., R. Muryanto, S.L. Vadas, and G. Crowley, 2010: "Periodic spacing between
687 consecutive equatorial plasma bubbles", Geophys. Res. Lett., submitted.

688 Medvedev, A.S. and N.M. Gavrilov, 1995: The nonlinear mechanism of gravity wave
689 generation by meteorological motions in the atmosphere, *J. Atmos. Terres. Phys.*,
690 **57**, 1221–1231.

691 Miyoshi Y. and H. Fujiwara, 2008: Gravity Waves in the Thermosphere Simulated by a
692 General Circulation Model, *J. Geophys. Res.*, **113**, D01101, doi:10.1029/2007JD008874.

693 Nakamura, T., A. Higashikawa, T. Tsuda, and Y. Matsushita, 1999: Seasonal variations of
694 gravity wave structures in OH airglow with a CCD imager at Shigaraki, *Earth Plan-*
695 *ets Space*, **51**, 897-906.

696 Nastrom, G. D., B. B. Balsley, and D. A. Carter, 1982: Mean meridional winds in the
697 mid- and high-latitude summer mesosphere, *Geophys. Res. Lett.*, **9**, 139–142.

698 Nicolls, M. J., R. H. Varney, S. L. Vadas, P.A. Stamus, C. J. Heinselman, R. B. Cosgrove,
699 and M. C. Kelley, 2010: "Case Study of an Inertia-Gravity Wave in the Mesosphere
700 over Alaska with the Poker Flat Incoherent Scatter Radar", J. Geophys. Res.Atmospheres,
701 to be submitted.

702 Oliver, W. L., Y. Otsuka, M. Sato, T. Takami, and S. Fukao, 1997: A climatology of
703 F region gravity wave propagation over the middle and upper atmosphere radar,
704 *J. Geophys. Res.*, **102**, 14,499–14,512.

Piani, C., D. Durran, M. J. Alexander, and J. R. Holton, 2000: A numerical study of three dimensional gravity waves triggered by deep tropical convection, *J. Atmos. Sci.*, **57**, 3689–3702.

Plougonven, R., A. Hertzog, and H. Teitelbaum, 2008: Observations and simulations of a largeamplitude mountain wave breaking over the Antarctic Peninsula, *J. Geophys. Res.*, **113**, D16, doi:10.1029/2007JD009739.

Richmond, A. D., 1978: Gravity wave generation, propagation, and dissipation in the thermosphere, *J. Geophys. Res.*, **83**, 4131–4145.

Stull R.B., 1976: Internal gravity waves generated by penetrative convection, *J. Atmos. Sci.*, **33**, 1279–1286.

Takahashi, H., M. J. Taylor, P.-D. Pautet, A. F. Medeiros, D. Gobbi, C. M. Wrasse, J. Fechine, M. A. Abdu, I. S. Batista, E. Paula, J. H. A. Sobral, D. Arruda, S. L. Vadas, F. S. Sabbas, and D. C. Fritts, 2009: Simultaneous observation of ionospheric plasma bubbles and mesospheric gravity waves during the SpreadFEx Campaign, *Ann. Geophys.*, **27**, 1477–1487.

Taylor, M. J., and M. A. Hapgood, 1990: On the origin of ripple-type wave structure in the OH nightglow emission, *Planet. Space Sci.*, **38**, 1421-1430.

Taylor, M. J., D. C. Fritts, and J. R. Isler, 1995: Determination of horizontal and vertical structure of an unusual pattern of short period gravity waves imaged during ALOHA-93, *Geophys. Res. Lett.*, **22**, 2837 2840.

Vadas, S. L., and D. C. Fritts, 2001: Gravity wave radiation and mean responses to local body forces in the atmosphere, *J. Atmos. Sci.*, **58**, 2249–2279.

Vadas, S. L., D. C. Fritts, and M.J. Alexander, 2003: Mechanism for the generation of secondary waves in wave breaking regions, *J. Atmos. Sci.*, **60**, 194–214.

Vadas, S. L, and D. C. Fritts, 2004: Thermospheric responses to gravity waves arising from mesoscale convective complexes, *J. Atmos. Solar Terres. Phys.*, **66**, 781–804.

731 Vadas, S. L., and D. C. Fritts, 2006: Influence of solar variability on gravity wave structure
732 and dissipation in the thermosphere from tropospheric convection, *J. Geophys. Res.*,
733 **111**, A10S12, doi:10.1029/2005JA011510.
734 Vadas, S.L., 2007: Horizontal and vertical propagation and dissipation of gravity waves
735 in the thermosphere from lower atmospheric and thermospheric sources, *J. Geo-*
736 *phys. Res.*, **112**, A06305, doi:10.1029/2006JA011845.
737 Vadas, S. L., and M. J. Nicolls, 2008: Using PFISR measurements and gravity wave
738 dissipative theory to determine the neutral, background thermospheric winds, *Geo-*
739 *phys. Res. Lett.*, **35**, L02105, doi:10.1029/2007GL031522.
740 Vadas, S. L., and M. J. Nicolls, 2009: Temporal evolution of neutral, thermospheric winds
741 and plasma response using PFISR measurements of gravity waves, *J. Atmos. So-*
742 *lar Terres. Phys.*, **71**, 740–770.
743 Vadas, S. L., and D.C Fritts, 2009: Reconstruction of the gravity wave field from convec-
744 tive plumes via ray tracing, *Ann. Geophys.*, **27**, 147-177.
745 Vadas, S. L., J. Yue, C.-Y. She, P.A. Stamus and A. Liu, 2009: A model study of the
746 effects of winds on concentric rings of gravity waves from a convective plume near Fort
747 Collins on 11 May 2004, *J. Geophys. Res.*, **114**, D06103, doi:10.1029/2008JD010753.
748 Vadas, S. L. and H.-L. Liu, 2009: The generation of large-scale gravity waves and neu-
749 tral winds in the thermosphere from the dissipation of convectively-generated gravity
750 waves, *J. Geophys. Res.*, **114**, A10310, doi:10.1029/2009JA014108.
751 Vadas, S.L. and G. Crowley, 2009: "Sources of the traveling ionospheric disturbances
752 observed by the ionospheric TIDDBIT sounder near Wallops Island on October 30,
753 2007" J. Geophys. Res., in press.
754 Vadas, S. L., 2010: "Compressible f-plane solutions to local body forces and heatings; Part
755 I: Initial value and forced/heated solutions" J. Geophys. Res.Atmospheres, submitted.
756 Waldock, J.A. and T.B. Jones, 1984: The effects of neutral winds on the propagation of

757 medium-scale atmospheric gravity waves at mid-latitudes, *J. Atmos. Terres. Phys.*,
758 **46**, 217–231.
759 Waldock, J.A. and T.B. Jones, 1986: HF doppler observations of medium-scale travelling
760 ionospheric disturbances at mid-latitudes, *J. Atmos. Terres. Phys.*, **48**, 245–260.
761 Walterscheid, R. L. and D. J. Boucher, Jr., 1984: A simple model of the transient response
762 of the thermosphere to impulsive forcing, *J. Atmos. Sci.*, **41**, 1062–1072.
763 Walterscheid, R. L., G. Schubert, and D. G. Brinkman, 2001: Small-scale gravity waves in
764 the upper mesosphere and lower thermosphere generated by deep tropical convection,
765 *J. Geophys. Res.*, **106,D23**, 31,825–31,832.
766 Yamada, Y., H. Fukunishi, T. Nakamura, and T. Tsuda, 2001: Breaking of smallscale
767 gravity wave and transition to turbulence observed in OH airglow, *Geophys. Res. Lett.*,
768 **28**, 2153-2156.
769 Zhu, X. and J. R. Holton, 1987: Mean fields induced by local gravity-wave forcing in the
770 middle atmosphere, *J. Atmos. Sci.*, **44**, 620-630.

## Figure Captions

Figure 1: Zonal velocity spectra for the GWs excited by a zonal body force which models wave breaking near the mesopause (solid). Contours show 10% intervals of the maximum value. a) Boussinesq solution. b) Compressible solution. The turquoise and red dots indicate those GWs where their momentum fluxes are maximum (i.e., $z_{\rm diss}$) for select $\lambda_H$ at $z = 150$ km and $z = 250$ km, respectively. Pink dash-dot lines indicate $c_{gz}$ at 5, 10, 15, 25, and 45 ms$^{-1}$, as labeled. Blue dash lines indicate the intrinsic horizontal phase speed $c_{IH}$ in 50 ms$^{-1}$ intervals. The green dashed lines show $\tau_{Ir} = 30$, 60, 90, and 120 min. The pink, blue and green lines use the anelastic GW dispersion relation for all spectral plots in this paper.

Figure 2: Density perturbations of the compressible solution, $\rho'/\overline{\rho}$, at $z = 150$ km excited by the zonal body forcing in Fig. 1b. Maximum positive (negative) values are white (black) for all images in this paper. a)-h) show the solutions at $t = 4$, 6, 10, 20, 30, 60, 90, and 120 min, respectively, with maximum values of 0.5, 2, 10, 9, 7, 7, 4, and 2%, respectively.

Figure 3: Meridional velocity spectra for the GWs excited by a meridional body force modeling a geostrophic adjustment of the jet stream (solid). Contours show 10% intervals of the maximum value. a) Boussinesq solution. b) Compressible solution. Pink dash-dot lines indicate $c_{gz}$ for 0.01, 0.1, 0.5, 1, and 2 ms$^{-1}$, as labeled. Blue dash lines indicate the intrinsic horizontal phase speed $c_{IH}$ in 25 ms$^{-1}$ intervals. The green dashed lines show intrinsic periods of $\tau_{Ir} = 3$, 7, 10 and 12 hr.

Figure 4: Zonal (solid) and meridional (dash) velocity perturbations from the geostrophic adjustment in Fig. 3b using the compressible solutions. a,c,e,g show vertical profiles at $x = x_0$ and $y = y_0 + 2550$ km. b,d,f,h show radial plots at $z = 35$ km and $x = x_0$. Rows 1-4 show the solutions at 24, 36, 48, and 60 hr, respectively.

Figure 5: Meridional velocity spectra for the GWs excited by meridional thermospheric body forces at $z = 150$ km (solid). Contours show 10% intervals of the maximum value. a) Boussinesq solution for $\mathcal{D}_z = 10$ km. b) Compressible solution for $\mathcal{D}_z = 10$ km. c) Boussinesq solution for $\mathcal{D}_z = 40$ km. d) Compressible solution for $\mathcal{D}_z = 40$ km. e) Boussinesq solution for $\mathcal{D}_z = 100$ km. d) Compressible solution for $\mathcal{D}_z = 100$ km. All solutions are scaled by the same value. The turquoise and red dots are the same as in Fig. 1. Pink dash-dot lines indicate $c_{gz}$ for 15, 30, 45, 60, 75, and 90 ms$^{-1}$. Blue dash lines indicate the intrinsic horizontal phase speed $c_{IH}$ in 50 ms$^{-1}$ intervals. The green dashed lines show intrinsic periods of $\tau_{Ir} = 15$, 30, 60, 90 and 120 min.

Figure 6: Density perturbations, $\rho'/\overline{\rho}$, at $z = 240$ km of the GWs and AWs from the body forces shown in Figure 5d and 5f. a)-d) $\mathcal{D}_z = 40$ km. e)-h) $\mathcal{D}_z = 100$ km. From left to right, the perturbations are shown at $t = 20$, 30, 60, and 90 min, respectively. The maximum values in a)-h) are 2.3, 2.2, 2.8, 1.4, 2.9, 1.8, 0.3, and 0.1%, respectively.

Figure 7: a)-c): $u'$, $v'$, and $w'$ at $z = 240$ km and $t = 30$ min for the thermospheric body force in Figure 5f. The maximum values in a)-c) are 6, 13, and 10 m/s, respectively.

Figure 8: GW spectra from a deep convective plume. Shown are the maximum GW horizontal velocity amplitudes at $z = 87$ km in m/s if the winds are zero (solid). a) Boussinesq solutions. b) Compressible solutions. The turquoise and red dots are the same as in Fig. 1. Pink dash-dot lines indicate $c_{gz}$ in 15 ms$^{-1}$ intervals. Blue dash lines indicate the intrinsic horizontal phase speed $c_{IH}$ in 50 ms$^{-1}$ intervals. The green dashed lines show $\tau_{Ir} = 10$ and 30 min.

Figure 9: GW and AW zonal and vertical velocity perturbations at $t = 15$ min and $y = y_0$ from the modeled convective plume in Figure 8b. Solid lines indicate positive values, and dash lines indicate negative values. a-d show the plume with $\chi = 10$ min. e-h show the plume with $\chi = 1$ min. a) GW $u'$. b) GW $w'$. c) AW $u'$. d) AW $w'$. e) GW $u'$. f) GW

820 $w'$. g) AW $u'$. h) AW $w'$. Perturbations are multiplied by $\exp(-(z-z_0)/2\mathcal{H})$. Contours
821 are 10, 30, 50, 70, and 90% of the maximum value. The maxima in a)-h) are 5.6, 6.0,
822 $2.9 \times 10^{-3}$, $7.8 \times 10^{-3}$, 17, 84, 0.62, and 1.0 m/s, respectively.

823 Figure 10: Temperature perturbations, $T'/\overline{T}$, at $z = 90$ km for the waves excited by
824 the plume in Figure 8b. These are the compressible solutions. a)-d) show the wave per-
825 turbations at $t = 6$, 7, 8, and 10 min, respectively, with maximum values of 2, 4, 7,
826 and 4%, respectively. e)-h) show the wave perturbations at $t = 20$, 40, 60, and 80 min,
827 respectively, with maximum values of 2, 19, 23, and 23%, respectively.

828 Figure 11: Zonal velocity spectra for the GWs excited by a Gaussian heating at $z = 140$
829 km (solid). Contours show 10% intervals of the maximum value. a) Boussinesq solution
830 for $\mathcal{D}_x = 10$ km. b) Compressible solution for $\mathcal{D}_x = 10$ km. c) Boussinesq solution for
831 $\mathcal{D}_x = 100$ km. d) Compressible solution for $\mathcal{D}_x = 100$ km. Solutions in each row are scaled
832 by the same value. The turquoise and red dots are the same as in Fig. 1. Pink dash-dot
833 lines indicate $c_{gz}$ in 15 $\mathrm{ms}^{-1}$ intervals. Blue dash lines indicate the intrinsic horizontal
834 phase speed $c_{IH}$ in 50 $\mathrm{ms}^{-1}$ intervals. The green dashed lines show $\tau_{Ir} = 15$, 30, 60, 90,
835 and 120 min.

836 Figure 12: Density perturbations, $\rho'/\overline{\rho}$, at $z = 250$ km excited by the Gaussian heating
837 from Figure 11b. a)-d) show the AW perturbations only at times $t = 4$, 5, 6, and 8 min,
838 respectively, with maximum values of 2, 2, 2, and 1%, respectively. e)-h) show the GW
839 perturbations only at times $t = 30$, 60, 90, and 120 min, respectively, with maximum
840 values of 4, 2, 3, and 4%, respectively.

841 Figure 13: Vertical velocity perturbations, $w'$ from a line-shaped heating with $D_x = 400$
842 km. a)-d) show the AW perturbations only at times $t = 4$, 5, 6, and 8 min, respectively,
843 with maximum values of 90, 60, 40, and 30 m/s, respectively. e)-h) show the GW per-
844 turbations only at times $t = 30$, 60, 90, and 120 min, respectively, with maximum values

of 50, 100, 140, and 160 m/s, respectively.

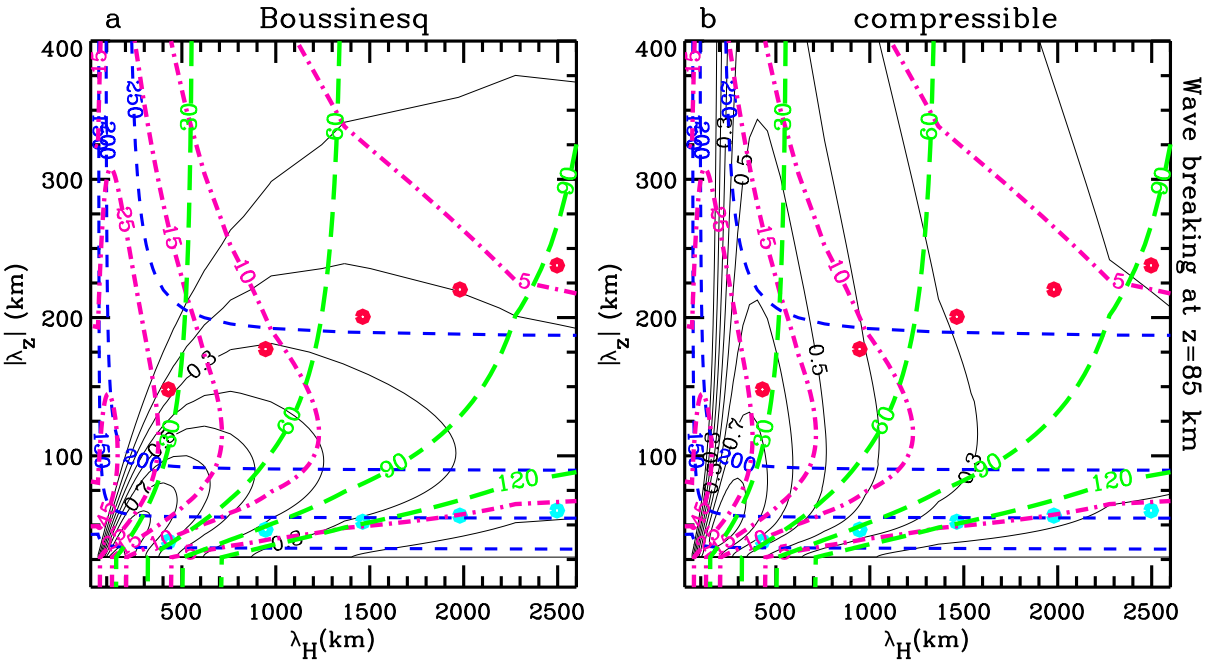


Figure 1:

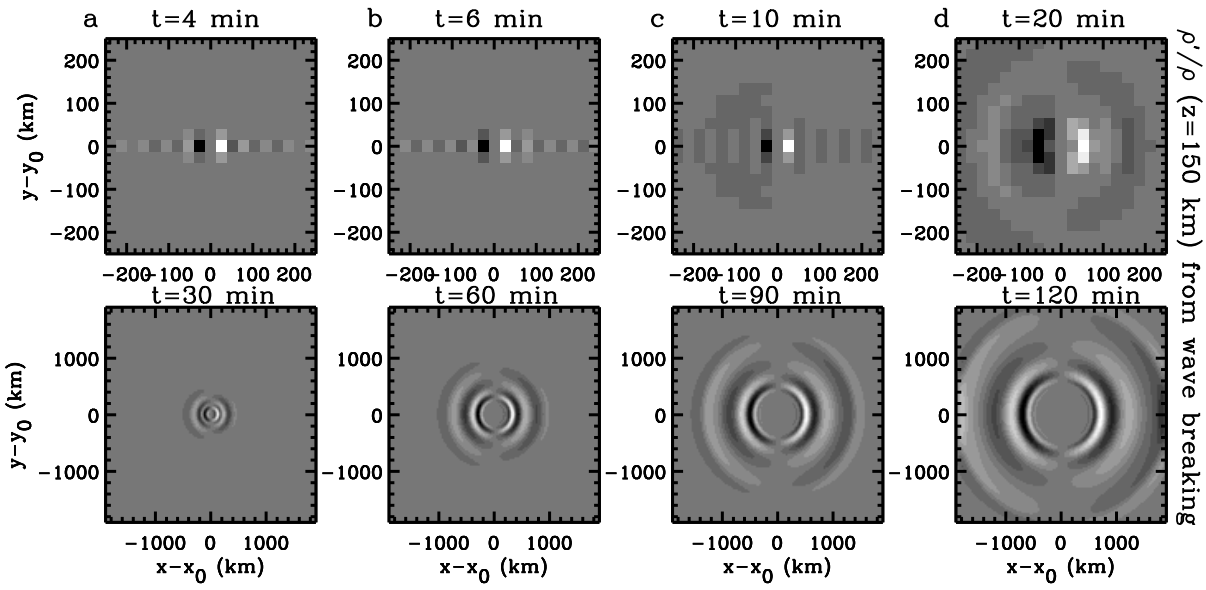


Figure 2:

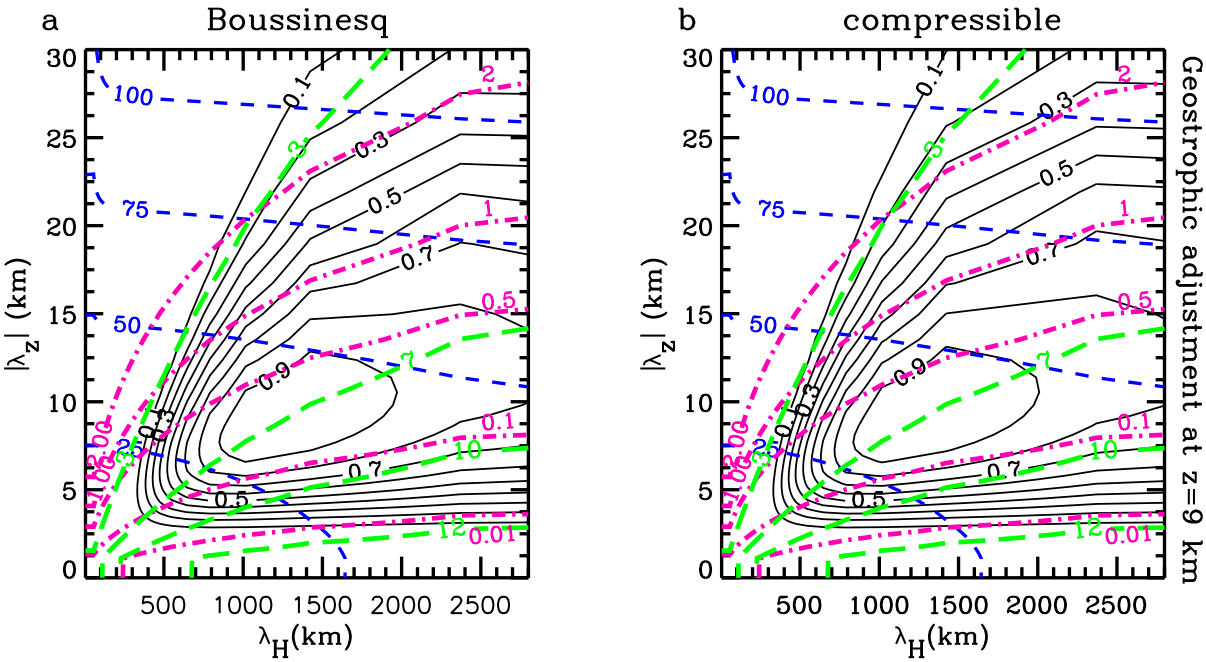


Figure 3:

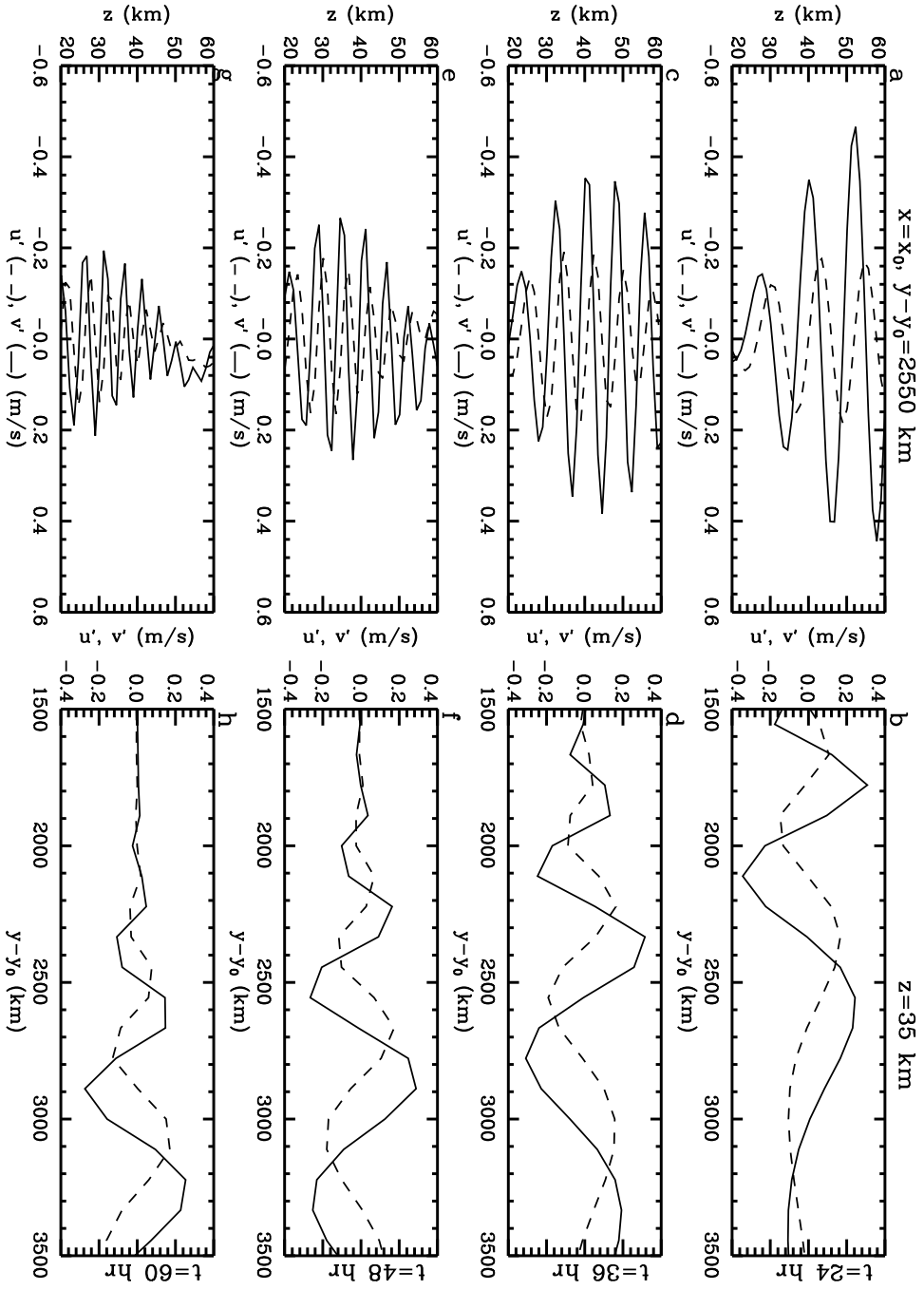
a
b
c
d
e
f
g
h
x=x0, y−y0=2550 km
z=35 km
z (km)
u′, v′ (m/s)
u′ (_ _), v′ (—) (m/s)
y−y0 (km)
t=24 hr
t=36 hr
t=48 hr
t=60 hr

Figure 4:

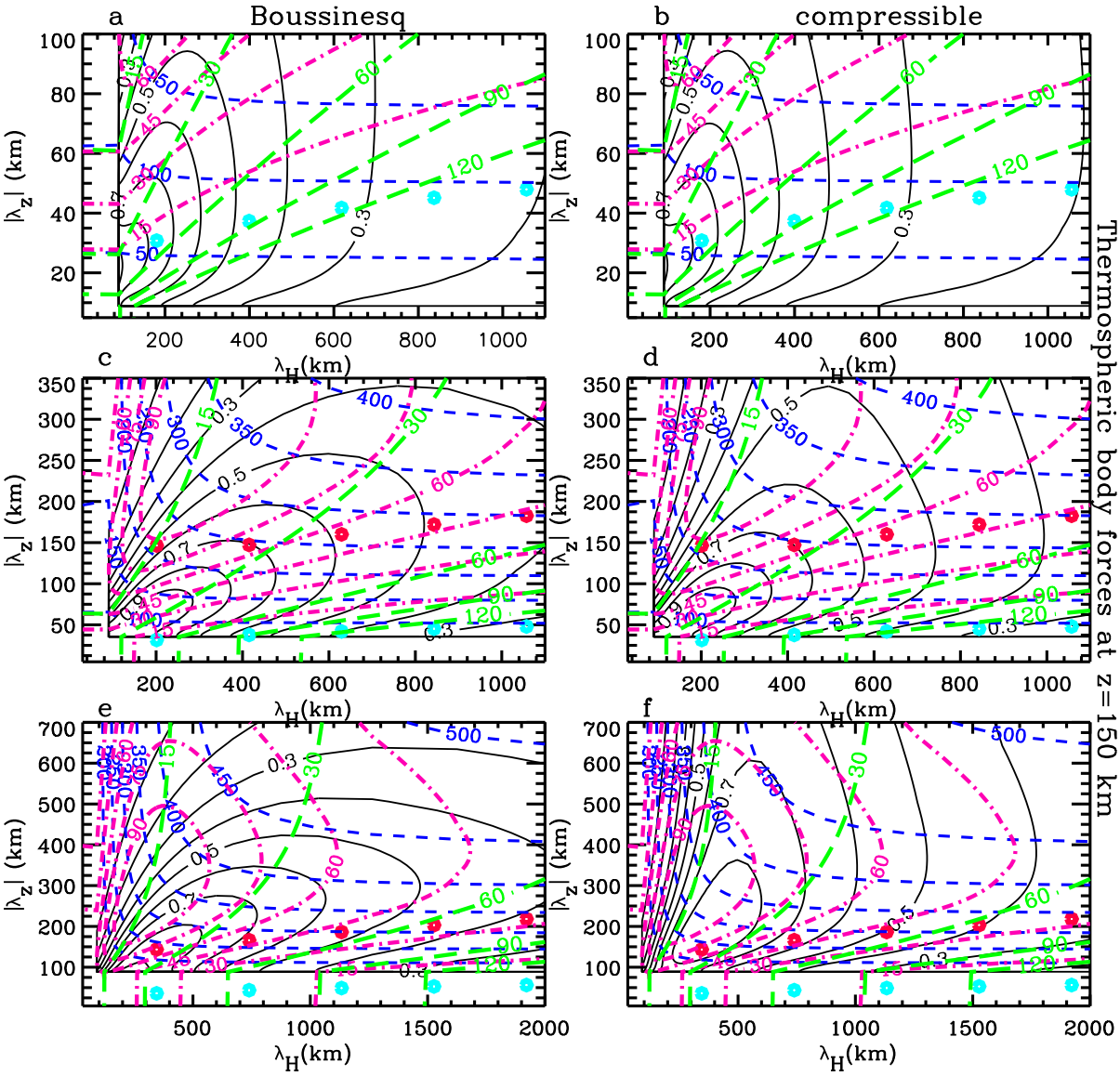
a
Boussinesq
b
compressible
c
d
e
f
|λz| (km)
λH(km)
Thermospheric body forces at z=150 km

Figure 5:

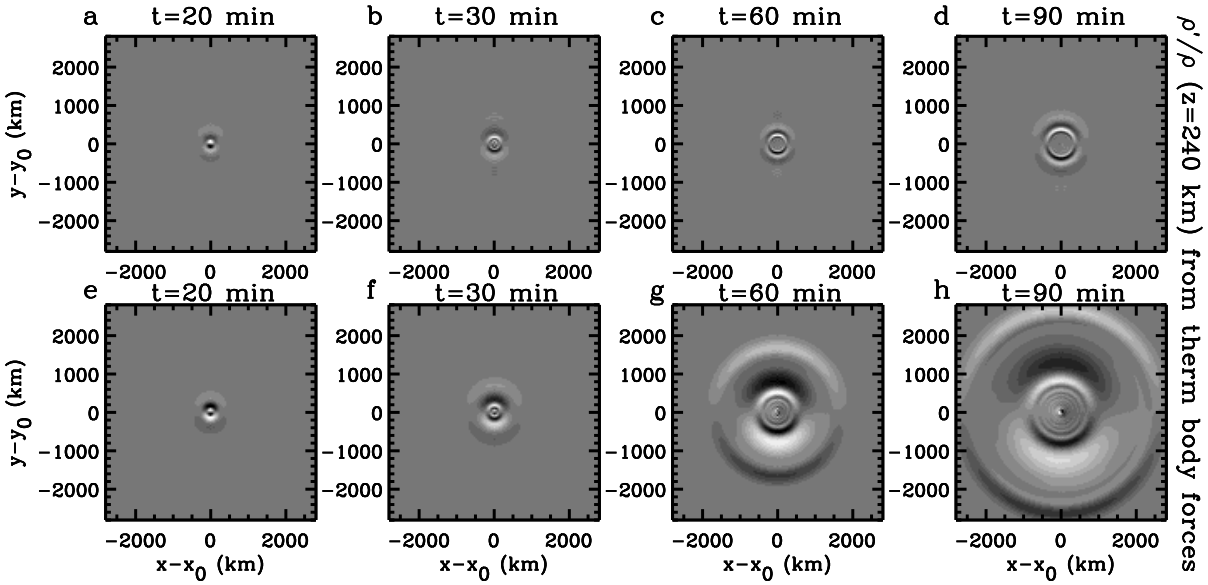


Figure 6:

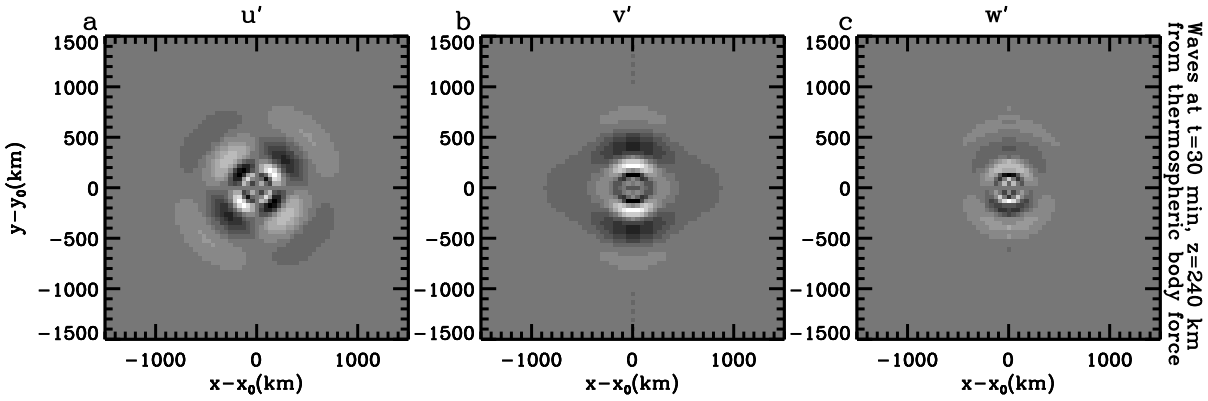


Figure 7:

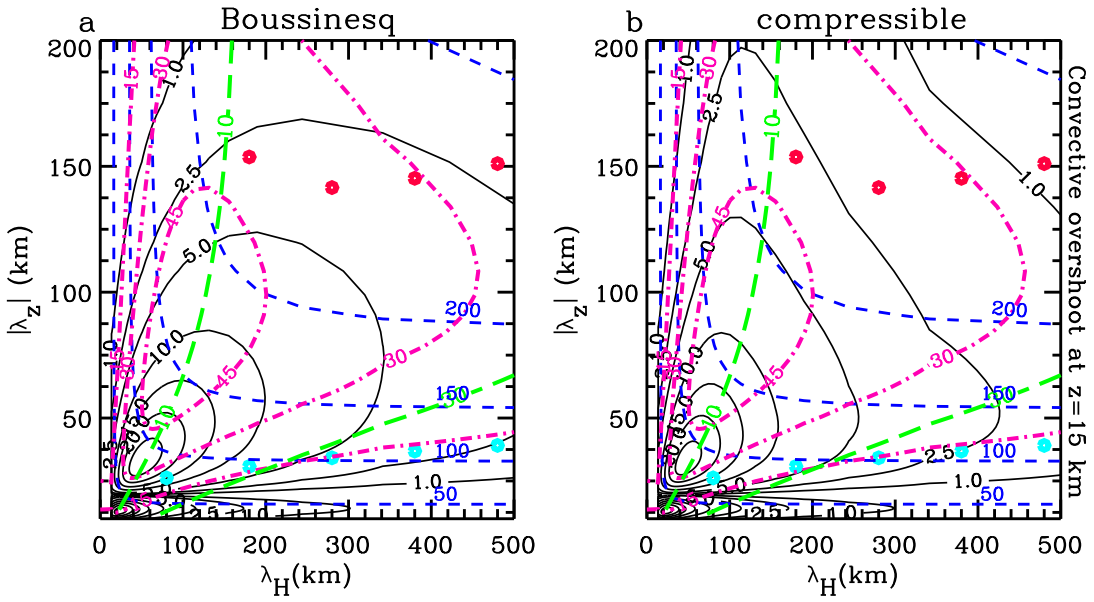
a
Boussinesq
b
compressible
Convective overshoot at z=15 km
|λz| (km)
λH(km)
200
150
100
50
0
100
200
300
400
500
1.0
2.5
5.0
10.0
15
30
45
50
100
150
200

Figure 8:

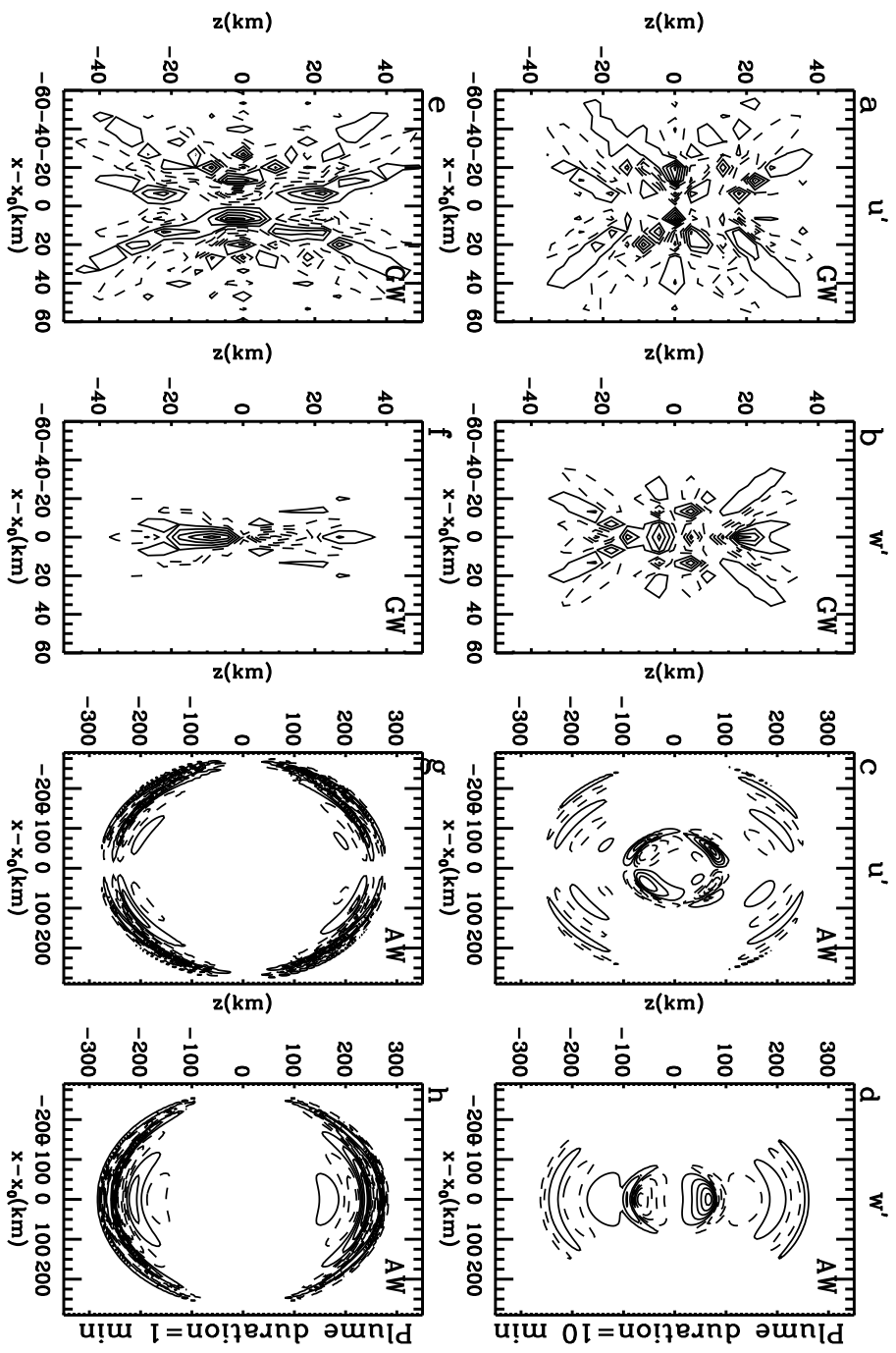
Plume duration=10 min
Plume duration=1 min
a u′
b w′
c u′
d w′
e
f
g
h
GW
AW
z(km)
x−x0(km)

Figure 9:

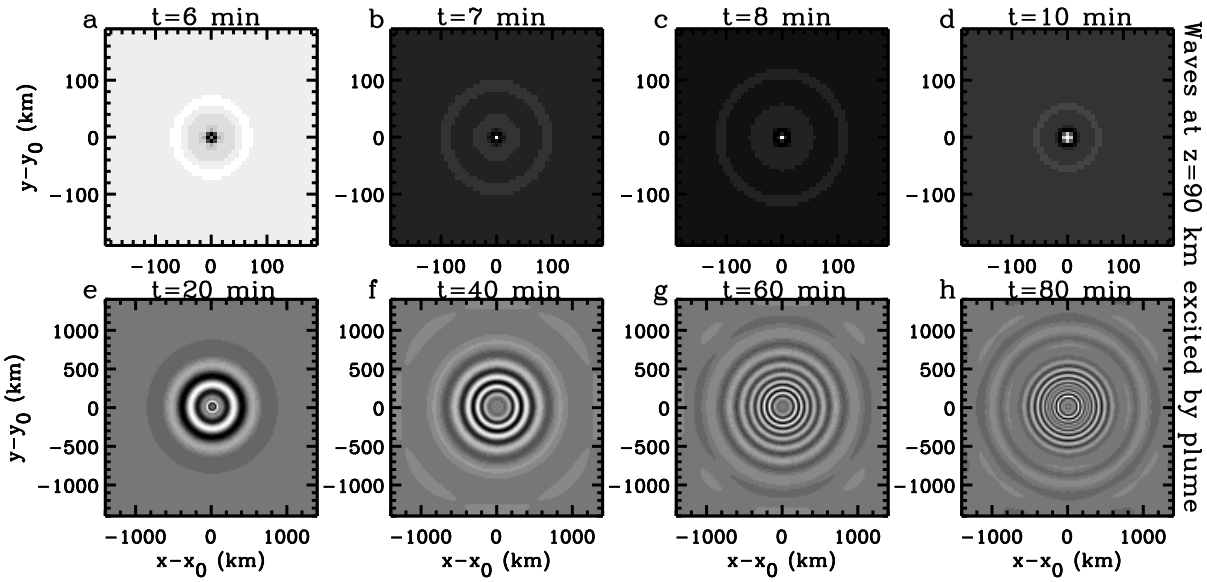


Figure 10:

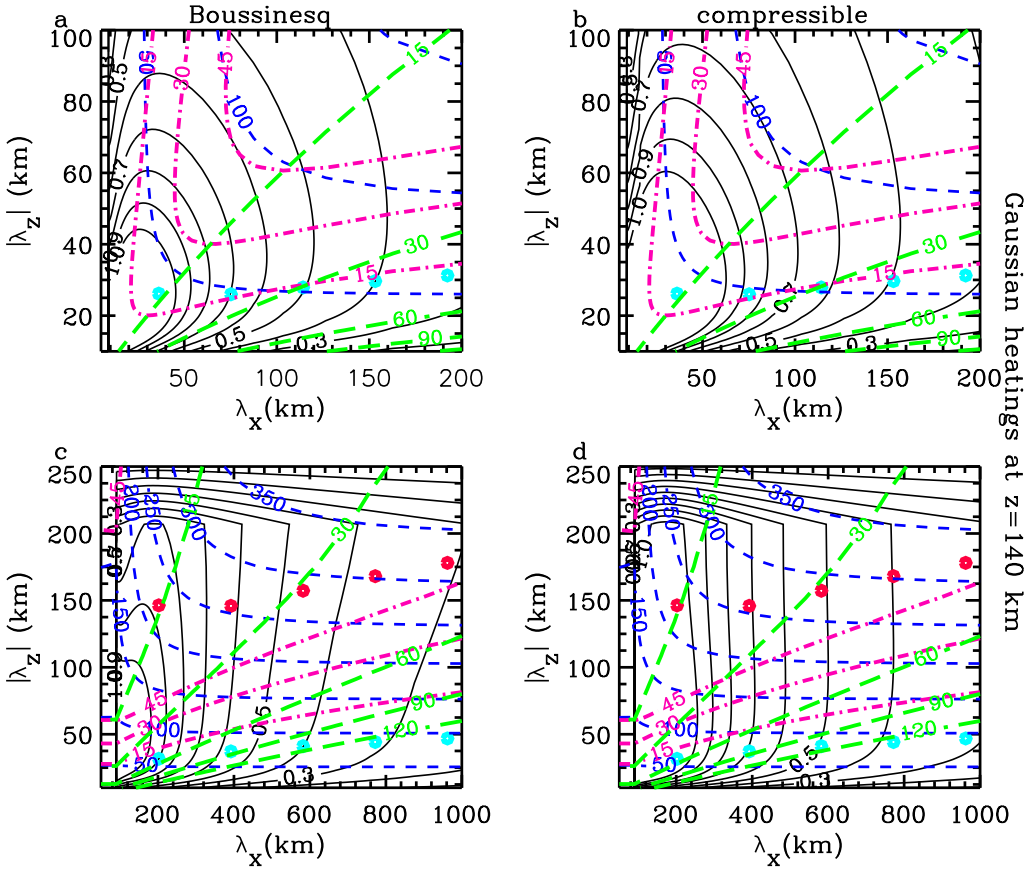


Figure 11:

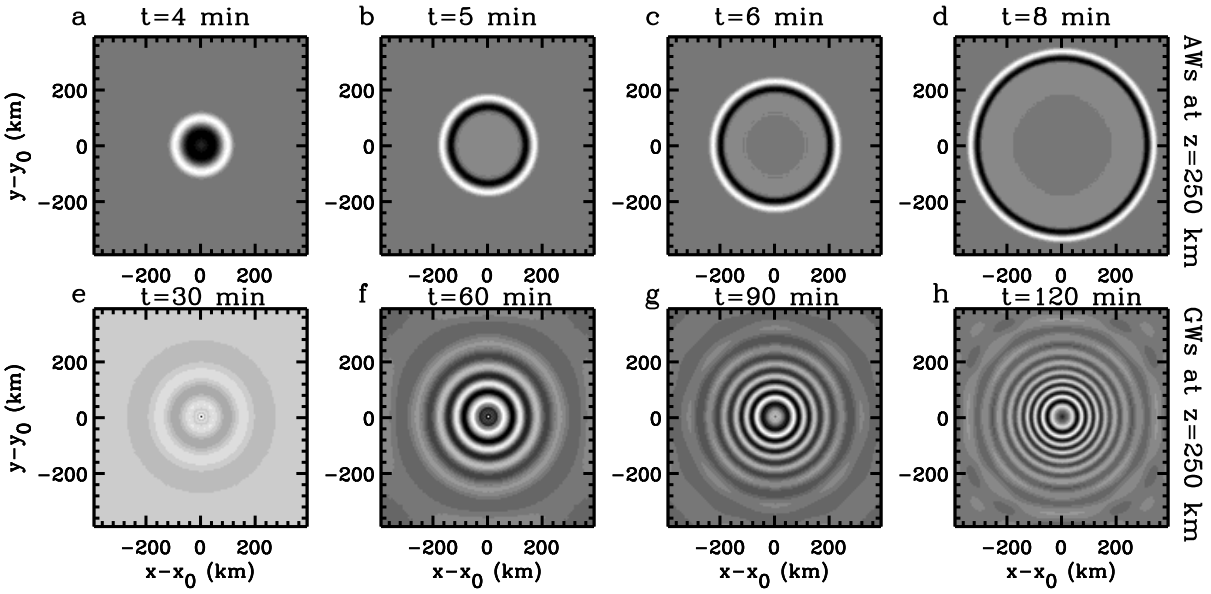


Figure 12:

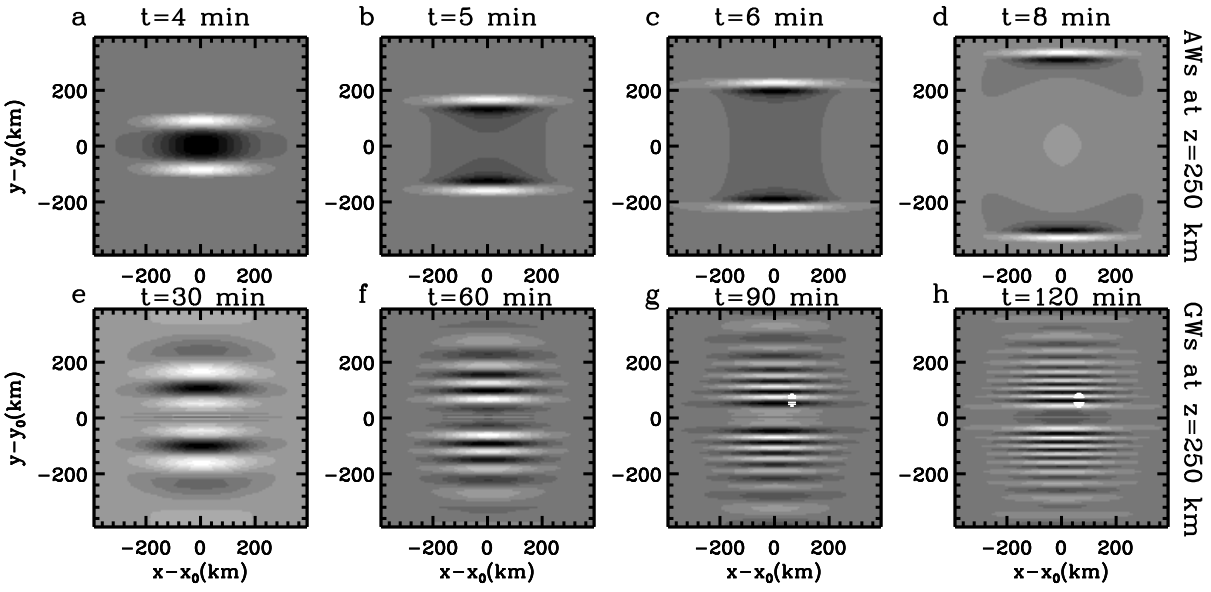


Figure 13: